Geochimica et Cosmochimica Acta 384 (2024) 44–64

Contents lists available at ScienceDirect

Geochimica et Cosmochimica Acta

journal homepage: www.elsevier.com/locate/gca

Systematic behaviour of $^{3}He/^{4}He$ in Earth's continental mantle

S.A. Gibson [a,*], J.C. Crosby [a], J.A.F. Day [a], F.M. Stuart [b], L. DiNicola [b], T.R. Riley [c]

[a] Department of Earth Sciences, University of Cambridge, Downing Street, Cambridge CB2 3EQ, UK
[b] Scottish Universities Environmental Research Centre, Rankine Avenue, East Kilbride G75 0QF, UK
[c] British Antarctic Survey, High Cross, Madingley Road, Cambridge CB3 0ET, UK

ARTICLE INFO

Associate editor: Manuel Moreira

Keywords:
Helium
Melt extraction
Earth evolution
Mantle xenolith
Peridotite
Pyroxenite
Kimberlite

ABSTRACT

Helium isotopes are unrivalled tracers of the origins of melts in the Earth's convecting mantle but their role in determining melt contributions from the shallower and rigid lithospheric mantle is more ambiguous. We have acquired new $^{3}He/^{4}He$ data for olivine and pyroxene separates from 47 well-characterised mantle xenoliths from global on- and off-craton settings. When combined with existing data they demonstrate a new systematic relationship between fluid-hosted $^{3}He/^{4}He$ and major and trace element composition of host minerals and whole rock. We show that a significant proportion (>70 %) of mantle peridotites from continental off-craton settings with depleted major element compositions (e.g., olivine Mg# ≥ 89.5) have $^{3}He/^{4}He$ in the range of modern-day mid-ocean ridge basalt (MORB) source mantle (7–9 R_a) and we propose that they represent underplated melt residues, which initially formed in the convecting upper mantle. Furthermore, we observe that off-craton mantle xenoliths with signatures often attributed to enrichment by melts or fluids from 'ancient' subducted oceanic lithosphere have lower $^{3}He/^{4}He$ (<7 R_a). Modest correlations between $^{3}He/^{4}He$ and whole rock incompatible trace element signatures commonly used as proxies for metasomatism by small-fraction carbonatite and silicate melts or C-O-H fluids characterise lithospheric mantle with $^{3}He/^{4}He$ ranging from 5 to 8 R_a.

Using a numerical model that integrates temperature-dependent melt extraction from the upper mantle with *in-situ* radiogenic ingrowth of ^{4}He in the continental mantle we show that the initial $^{3}He/^{4}He$ of continental lithosphere mantle has decreased over time. This is consistent with previous observations demonstrating that ancient (2.5–3.5 Ga) cratonic mantle has a depleted mineral chemistry (e.g., olivine Mg# = 91–94) and low $^{3}He/^{4}He$ (0.5–6.7 R_a), while continental off-craton mantle (<2.5 Ga) is more fertile (olivine Mg# = 88–92) and has less radiogenic $^{3}He/^{4}He$ (4–8.8 R_a). This relationship defines a 'global lithospheric mantle array' for intraplate peridotites on plots of $^{3}He/^{4}He$ vs olivine Mg#. Peridotites influenced by past and present subduction fluids, including those that contain amphibole, plot off this array. Our findings have broad implications for the $^{3}He/^{4}He$ signatures observed in continental magmas. Many of Earth's deepest melts, i.e. proto-kimberlites, are characterised by relatively low $^{3}He/^{4}He$. We attribute this to assimilation and incorporation of low $^{3}He/^{4}He$ cratonic mantle material during ascent of carbonate-rich melts through thick lithosphere, which overprints the original signatures. Moreover, our findings suggests that the lithospheric mantle acts as a long-term reservoir for other fluid-hosted volatiles (e.g., CO_2, CH_4, H_2O), and in some cases able to sequester these over billion-year timescales until physio-chemical perturbation (e.g., during major rifting or heating events).

1. Introduction

Earth's rigid lithospheric mantle and the underlying convecting mantle are dominated by peridotite but over the course of geological time these reservoirs have evolved independently to have distinct chemical compositions and isotopic signatures (McKenzie and Bickle, 1988). The lithospheric mantle occupies 2 % of the total mass of bulk silicate Earth and its location at the interface between the convecting mantle and crust makes it a critical reservoir in geochemical cycles (Gibson and McKenzie, 2023). The long and often complex evolution of the continental lithospheric mantle has been established from the compositions of small-fraction melts generated during major heating and rifting events (kimberlites, lamprophyres etc) and also from their xenolith cargo (e.g., Pearson and Wittig, 2014 and references therein). Major- and trace-elements together with Sr, Nd, Hf and Os isotopes of this entrained material show that the continental lithospheric mantle

* Corresponding author.
E-mail address: sally@esc.cam.ac.uk (S.A. Gibson).

https://doi.org/10.1016/j.gca.2024.09.009
Received 19 December 2023; Accepted 4 September 2024
Available online 7 September 2024

initially formed as residues of melting in the convecting mantle (e.g., (Walker et al., 1989; Pearson et al., 1995b, 1995a; Herzberg, 2004; Simon et al., 2007; Gibson, 2008; Pearson and Wittig, 2014: 201; Oller et al., 2022). Following segregation of these residues from the convecting mantle and accretion to the lithosphere, the continental mantle has experienced numerous phases of metasomatic enrichment (e.g., Shu et al., 2019). This has involved the percolation and crystallisation or reaction of small-fraction volatile-rich melts and fluids, derived from

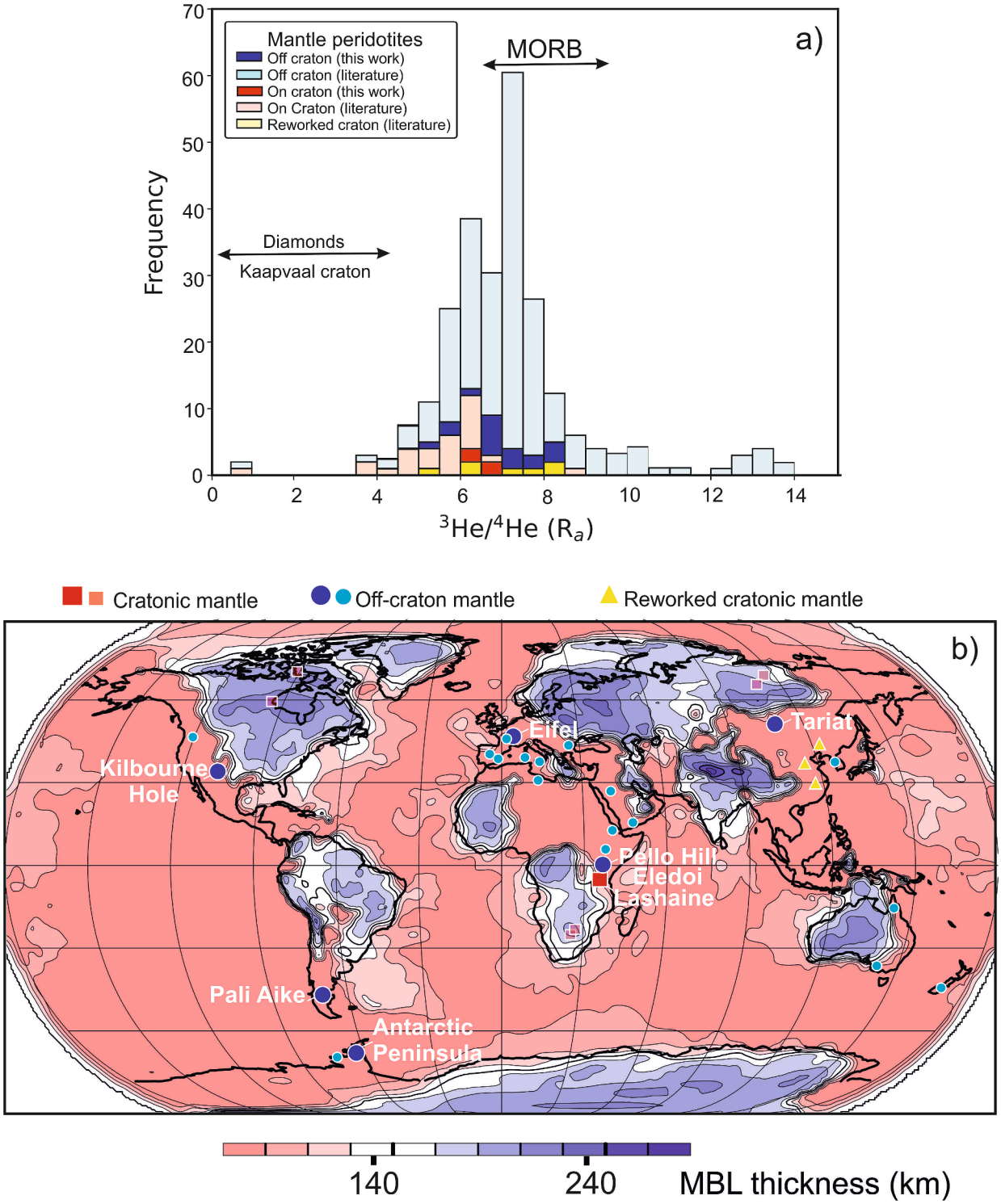

Fig. 1. (a) Histogram of $^3He/^4He$ ratios for mantle peridotites from on- and off-craton settings together with the ranges of observed in MORB and diamonds. (b) Locations of peridotite and pyroxenite xenoliths analysed in this study (large symbols) for $^3He/^4He$ superimposed on a map of mechanical boundary layer thickness (Priestley and McKenzie, 2013). Locations (smaller symbols) are also shown for on- and off-craton mantle xenoliths referred to in our study. Data are from: this work; (Matsumoto et al., 1998; Dodson and Brandon, 1999; Hoke et al., 2000; Gautheron and Moreira, 2002; Graham, 2002; Gautheron et al., 2005; Kim et al., 2005; Sapienza et al., 2005; Czuppon et al., 2009; Nardini et al., 2009; Beccaluva et al., 2011; Martelli et al., 2011; Correale et al., 2012, 2015, 2019; Halldórsson et al., 2014; Su et al., 2014; Barry et al., 2015; Sgualdo et al., 2015; Jalowitzki et al., 2016; Konrad et al., 2016; Berkesi et al., 2019; Day et al., 2019; Kobayashi et al., 2019; Xu et al., 2019; Faccini et al., 2020; Barry and Broadley, 2021; Rizzo et al., 2021; Weiss et al., 2021).

the convecting mantle or subducted oceanic lithosphere, with the host peridotite (e.g., McKenzie, 1989; O'Reilly and Griffin, 2013). Rhenium-osmium isotopes have shown that the most ancient lithospheric mantle (>2.5 Ga) is found beneath Earth's cratons (Walker et al., 1989; Pearson et al., 1995b, 1995b). This is more depleted in magmaphile elements, such as Fe, Ca and Al, than the surrounding younger and thinner off-craton mantle. The more refractory nature of cratonic mantle is thought to reflect its formation by relatively large amounts of partial melting (>25 %) in the convecting mantle due to the higher mantle potential temperatures in the Archean when cratonic mantle formed (Richter, 1988; Tainton and McKenzie, 1994; Herzberg, 2004; Gibson, 2008). Despite recent advances in our understanding of the volatile inventory of the continental lithospheric mantle (e.g., Gibson et al., 2020; Gibson and McKenzie, 2023) the source of volatiles species and the mechanism for their incorporation remain poorly understood.

Helium isotopes have proved to be unrivalled as tracers of the structure and evolution of the convecting mantle (e.g., Class and Goldstein, 1997; Graham, 2002; Stuart et al., 2003; Porcelli and Elliott, 2008), as well as being crucial for tracking the inventory of major volatile species such as CO_2 (e.g., Marty and Tolstikhin, 1998). In the lithospheric mantle, helium is predominantly located in melt and CO_2-rich inclusions trapped in minerals that formed during crystallisation or subsequent melt/fluid-rock reactions, i.e. metasomatism (Trull and Kurz, 1993; Dunai and Porcelli, 2002; Gautheron and Moreira, 2002). Importantly, the generation of variable $^3He/^4He$ in minerals with different U/He ratios co-existing in the lithospheric mantle will be offset by the fast rates of helium diffusion (Trull and Kurz, 1993). While the inclusions may be subject to high-temperature sub-solidus chemical re-equilibration and deformation, mineral-melt partitioning experiments have determined that noble gases will overwhelmingly remain within fluids during this re-equilibration (e.g., Heber *et al.*, 2007). Additionally, deformation experiments on ultramafic minerals reveal that fluid inclusions are resistant to decrepitation (Yamamoto et al., 2011), although they will not survive the shearing and recrystallization that is often observed in kimberlite-borne xenoliths (Mercier and Nicolas, 1975; Heckel et al., 2022).

Previous studies have suggested that off-craton lithospheric mantle is characterised by a narrow range in $^3He/^4He$ (5–8 R_a; Fig. 1a) with a mean value of 6.1 ± 0.9 R_a (e.g., Gautheron and Moreira, 2002), where R_a is the atmospheric $^3He/^4He$ of 1.38 × 10^{-6}. This is lower than the mean $^3He/^4He$ of MORB (8 ± 1.5 R_a; Graham, 2002) and it has been hypothesized to be a consequence of higher concentration of U and Th in the lithospheric mantle that has generated more ^4He than the underlying convecting mantle (Dunai and Porcelli, 2002). More recent investigations of lithospheric peridotites and eclogites from a diverse range of tectonic settings have demonstrated a wider variation in $^3He/^4He$ (0.07–13.9 R_a; Halldórsson et al., 2014; Day et al., 2015) that has improved constraints on the origin of the melts that have enriched the continental lithospheric mantle (e.g., subducted lithosphere, MORB-source mantle, deep mantle). These studies also highlight how the He isotope composition of ancient continental mantle is complicated by the ingrowth of radiogenic He in xenolith minerals after crystallisation (Day et al., 2015). The processes that enrich strongly incompatible trace elements (e.g., Th and U) in the lithospheric mantle may also enrich helium (Reid and Graham, 1996), although others have argued that the He isotopic ratio of continental mantle reflects its initial $^3He/^4He$, Th/U and U/He ratios, age and degassing processes since its isolation from the depleted mantle (Dodson et al., 1998). Recently, it has been proposed that the addition of helium to continental mantle by melts derived from the underlying convecting mantle or by the ingrowth of U and Th after metasomatism results in low $^3He/^4He$ (Day et al., 2005, 2015). The extent to which ingrowth and metasomatism have biased our perception of the $^3He/^4He$ of continental mantle as recorded by analysis of xenolith minerals is still unclear (Day et al., 2015).

To advance our understanding of how well $^3He/^4He$ in peridotite xenoliths tracks the origin and subsequent metasomatic history of the continental lithospheric mantle we focus on relationships with mineral and whole-rock major and trace element composition that act as proxies for melt depletion and enrichment. This approach is currently limited by the availability of mantle xenoliths with combined $^3He/^4He$, major and trace element data, and mineral modal abundances (e.g., (Martelli et al., 2011; Correale et al., 2015; Day et al., 2015; Konrad et al., 2016; Xu et al., 2019; Faccini et al., 2020; Gibson et al., 2020; McIntyre et al., 2021; Rizzo et al., 2021; Zhang et al., 2022). Here, we present new measurements of melt/fluid inclusion-hosted $^3He/^4He$ in well-characterised peridotite and pyroxenite mantle xenoliths entrained from on- and off-craton continental mantle (Fig. 1b). We use these data to show how, to a first order, the $^3He/^4He$ of trapped fluids vary with the time of formation of the continental lithospheric mantle and demonstrate how incorporation and assimilation of this material can impact the $^3He/^4He$ of continental magmas.

2. Samples

We have determined $^3He/^4He$ of minerals from 47 peridotite and pyroxenite mantle xenoliths from N. Tanzania (Lashaine, Pello Hill and Eledoi); Antarctic Peninsula; Germany (W. Eifel); SW USA (Kilbourne Hole); Argentina (Pali Aike) and Mongolia (Tariat) (Table 1). The xenoliths are all from off-craton locations except those from Lashaine which are from the rifted eastern margin of the Tanzania craton (e.g., Gibson et al., 2013). The xenoliths were chosen because they are: (i) petrographically fresh, i.e. have translucent grains of olivine and all phases are free of alteration; (ii) were entrained by alkali basalts or olivine meliltites in the last 10 Myr; and (iii) have a wide range in modal mineralogy including spinel- and garnet-bearing lherzolites, harzburgites and pyroxenites (Table 1 & Figure S1 in the Supplementary Material). Pargasitic amphibole is present in three samples (DW10 and MM11 from the West Eifel, and L7.201.1.41 from the Antarctic Peninsula) and phlogopite mica is presents in four samples (L7.201.1.41 from the Antarctic Peninsula, CP62 from Pali AIke, and BD738 and BD816 from N. Tanzania (see Supplementary Material). The xenoliths display a wide variety of textures (Figs. S2-S5 in the Supplementary Material). Using terminology from Mercier and Nicolas (1975), these textures range from proto-granular, which is common in the Kilbourne Hole and Tariat peridotites, to porphyroclastic, equigranular (tabular and mosaic), and poikiloblastic that are more abundant at other locations. Our study focused on the larger (>2 mm in length), first generation of crystals, rather than the smaller grains that typically form as a result of shearing and recrystallisation (i.e. neoblasts). In order to overcome inter-mineral and whole-rock inconsistencies, our study only included chemically-equilibrated and near-equilibrated mantle xenoliths.

3. Analytical methods

3.1. Major element analysis

In-situ analyses of major element composition of olivine, clinopyroxene, orthopyroxene, spinel and garnet were undertaken on a Cameca SX-100 EMPA equipped with five WDS and one EDS detectors at the Micro-Analysis and Micro-Diffraction laboratory in the Department of Earth Sciences at the University of Cambridge. An accelerating voltage of 15 keV, and a current of 20nA was used with a beam size of 1 μm. Standards for calibration were Na on jadeite, K on K-feldspar, Fe on Fayalite, Mn, Ni, and Cr on pure metals, Si and Ca on diopside, Al on corundum, Mg on St Johns olivine, and Ti on rutile. San Carlos olivine, Aug12214, and VG2 glass were used as secondary standards. Matrix effects were corrected using the ZAF correction. For each sample, a minimum of three grains of each phase was analysed. The data reported are the average of these analyses with the uncertainties reported as standard deviations. Full major element analyses for olivine, orthopyroxene, clinopyroxene, spinel, garnet, amphibole, phlogopite and ilmenite are presented in Tables S2-9 in the Supplementary Material.

Table 1
Summary of the locations, mineral and whole-rock chemistry, and $^3He/^4He$ (R_a) of mantle xenoliths analysed in this study.

Sample	Ω Rock Type	Orthopyroxene		Olivine	Clinopyroxene		Spinel	Calculated Whole-Rock						
		Mg#	Al_2O_3	Fo	Mg#	[Ti/Eu]$_N$	Cr#	$^3He/^4He$ (Ra) *	Error	MgO	FeO^+	SiO_2	[La/Yb]$_N$	[Th/Yb]$_N$
Off craton														
West Eifel														
DW3	Lherzolite	92.1	2.79	91.7	92.11	0.05	39.9	6.8	0.2	44.8	7.3	42.4	36.44	26.59
DW7	Harzburgite	91.1	4.61	90.9	90.44	0.50	31.2	5.9	0.1	40.5	7.1	46.6	3.26	2.36
DW8	Lherzolite	91.6	2.93	91.2	92.14	0.23	24.1	5.9	0.2	43.1	7.6	43.4	41.61	87.30
DW10	Wehrlite + amph			89.4	90.84	0.09	42.5	6.7	0.1	37.8	7.9	43.3	16.67	8.22
G17	Lherzolite + amph	91.3	2.24	91.3	90.77	0.33	37.5	5.5	0.1	44.5	7.7	45.1	48.76	55.43
G18	Harzburgite + amph	91.1	2.87	91.1	92.01	0.76		5.3	0.2	44.5	7.7	45.7	21.65	45.46
MM5	Lherzolite	91.4	3.35	91.1	91.10	0.19	35.6	6.7	0.1	43.9	7.8	43.5	15.01	9.47
MM8	Harzburgite	91.7	3.67	91.4	91.06		45.1	6.3	0.1	46.2	7.7	43.5	11.69	4.47
MM11	Lherzolite	90.8	3.44	90.4	90.67	0.05	27.6	6.6	0.1	38.1	7.1	46.2	31.44	22.19
DW5	Pyroxenite			87.3	86.67			5.6	0.1	22.3	5.4	48.6		
MM6	Pyroxenite	89.1	4.08	88.4	87.99	0.68	45.1	6.6	0.2	31.3	7.4	45.2	7.55	2.33
Kilbourne Hole														
KH2	Lherzolite	89.7	4.88	89.2	89.69	0.67	9.9	7.1	0.4	38.7	8.3	43.6	0.19	2.40
KH3D	Lherzolite	91.3	4.31	90.9	90.75	0.52	39.8	7.8	0.2	44.5	7.8	44.6	1.98	2.39
KH4	Lherzolite	89.5	4.92	89.3	89.55	0.61	10.2	7.9	0.4	38.3	8.0	44.8	0.16	0.19
KH5	Lherzolite	89.2	4.89	89.3	89.97	0.60	9.0	7.3	0.3	38.8	8.1	45.3	0.16	0.19
KH1	Pyroxenite			79.9	78.70	0.96		7.7	0.1					
Tariat Depression														
TM1	Lherzolite	90.3	4.35	89.6	91.54	0.75	9.4	8.3	0.4	40.4	8.2	42.9	0.70	0.37
TM2	Lherzolite	90.1	4.73	89.5	90.26	0.65	10.7	8.0	0.2	43.1	8.9	43.8	0.93	0.30
TM3	Lherzolite	89.6	4.90	88.9	89.55	0.64	8.7	8.1	0.4	37.5	8.2	44.0	1.40	1.36
TM4	Lherzolite	90.9	4.00	90.3	92.00	1.01	13.3	7.6	0.1	39.5	7.6	43.8	0.70	0.37
Antarctic Peninsula														
BN	Lherzolite	89.7	4.09	89.3	90.90		9.9	7.3	0.2					
KG3609.21	Harzburgite	91.5	2.05	90.8	93.40		46.6	7.1	0.7					
KG3610.10A	Harzburgite	91.8	2.55	91.3	93.82	0.06	58.9	7.2	0.4	45.6	7.3	44.1	33.41	75.94
KG3719.25	Lherzolite	90.3	4.24	89.7	90.90		16.5	5.6	0.1					
L7.201.1.41	Lherzolite + amph	89.9	4.28	89.4	90.29	0.34	16.5	6.8	0.2	40.1	8.5	44.1	7.69	9.44
KG3619.7	Pyroxenite	81.0	4.95	79.4	80.40			6.8	0.2					
L7201.1.74c	Pyroxenite			81.1	78.00	0.97	0.0	6.5	0.1	41.6	15.8	7.7	3.57	15.74
R5194.2I	Pyroxenite			78.4	80.04	0.77	0.8	5.8	0.1	40.0	17.8	9.7	4.37	
R5194.2M	Pyroxenite				78.26	0.66	1.8	6.7	0.1	45.5	13.2	6.9	4.76	
Southern Patagonia														
CP31	Lherzolite							6.6	0.1					
CP33	Lherzolite	90.5	3.50	89.8	90.13		29.7	7.0	0.2	39.9	8.1	45.0		
LT1	Lherzolite	90.5	4.52	90.3	92.75	0.61	17.9	6.9	0.1	44.3	7.7	44.5	0.48	
LT16	Harzburgite	91.6	2.75	91.0	91.25	0.27	52.8	6.6	0.1	36.2	6.7	46.8	1.25	
PA3-5	Harzburgite	92.4	2.86	92.0			55.8	6.6	0.1					
CP62	Pyroxenite	87.3	3.42	86.2				7.2	0.1					
LT14	Pyroxenite	91.02	3.9		91.18		26.3	7.3	0.2	23.2	3.9	52.9		
LT15	Pyroxenite			83.6	87.56			6.7	0.1	18.1	4.5	50.3		
Craton margin														
Northern Tanzania														
BD128A	Peridotite							7.2	0.1					
BD730	Lherzolite	92.2	1.08	91.1	93.44	0.32	13.1	6.3	0.1	42.1	7.1	44.4	25.34	52.43
BD738	Lherzolite	93.0	1.10	92.1	93.44	0.37		6.7	0.3	43.5	6.8	44.1		
BD797	Harzburgite	93.6	1.27	92.5	92.93		71.4	6.3	0.1	44.3	6.1	45.0	39.30	68.63
BD822	Harzburgite	93.5	1.78	92.5			72.9	6.5	0.1	46.5	6.8	42.4	87.59	205.88
BD816	Pyroxenite	85.2	0.39	82.0	93.55			6.2	0.1					
BD3847	Pyroxenite			82.9	84.35		63.7	6.9	0.1					

*Calculated using a weighted average of mineral phase.
$^+$Calculated using the method of Canil et al. (1994).
N denotes normalised to depleted MORB mantle (Salters and Stracke, 2004).
Full data sets are in the Supplementary Material.

Standard deviation of analysed samples for major elements are <0.3 wt % and detection limits were < 500 ppm.

3.2. Trace element analysis

In-situ trace element analysis was undertaken by Laser Ablation Inductively Coupled Plasma Mass Spectrometry (LA-ICP-MS) in the Department of Earth Sciences at the University of Cambridge. This

involved using a New Wave UP213 Nd:YAG laser ablation system attached to a Perkin-Elmer Elan DRC II ICP-MS system. Clinopyroxene, garnets, and amphiboles were analysed using CaO and SiO_2 from EMPA analysis as internal standards. Calibration and drift corrections were obtained using NIST 614, while NIST612, NIST610, BCR-2G, BIR-1G, and BHVO-2G were also used. Pure helium was used as the ablation gas at 700 mL min^{-1}. Ablated sample material was carried in helium gas, which was joined with the argon nebulised gas line from the ICP-MS using a signal homogenised device at 0.8 L min^{-1} before the ICP-MS torch. The NWR193 is equipped with a TwoVol2 sample chamber and small volume sample cup to quickly and efficiently transfer samples and washout performance.

Data was processed using Glitter software (GEMOC, Australia). The results were checked and filtered for background and melt/mineral inclusions after each analysis to optimise the data. Accuracy is good for data with results between 80 % and 120 % (Table S10 in the Supplementary Material). Rare-earth elements (REEs) were particularly accurate, with results between 80 % and 100 % accuracy. During analysis, suitable replicate spots were analysed and LA-ICP-MS results were averaged (Table S11 and 12 in the Supplementary Material). The spots were carefully chosen to avoid contamination from nearby cracks, inclusions, or any overlapping neighbouring phases to ensure only the targeted phase was analysed. For additional details, see Gibson et al. (2020).

3.3. Helium isotope analysis

Thin sections of all the xenoliths were initially screened using both optical and scanning electron microscopy to ensure that the constituent mineral phases are fresh and free of fractures. Small, rounded, isolated fluid inclusions are visible in the cores and along cross-cutting healed fracture planes in many of the olivine and pyroxene crystals (Fig. S2e in the Supplementary Material). Both types of fluid inclusions are indicative of their formation in the mantle (e.g., Andersen and Neumann, 2001).

Rock samples were mechanically disaggregated using a rock crusher in the Department of Earth Sciences, University of Cambridge. Olivine, orthopyroxene and clinopyroxene were handpicked from the crushate using an binocular microscope. The grains were then washed with distilled water, ultrasonicated in dilute HNO_3 for 15 min and washed with acetone.

Helium isotope measurements were made using a ThermoFisher Scientific Helix SFT dual collector mass spectrometer at the Scottish Universities Environmental Research Centre following the methods of Carracedo et al. (2019). Approximately 1 g of each mineral was loaded into an all-metal multi-sample hydraulic crusher. The system was pumped to ultra-high vacuum then baked for > 24 h at 80 °C. The gases were released by *in vacuo* crushing in a multi-sample hydraulic crusher (Stuart et al. 2000). The released gases were purified in an all-metal ultra-high-vacuum line equipped with two heated (250 °C) SAES GP50 getters and an activated charcoal finger (cooled to approximately −196 °C using liquid nitrogen). ^3He was analysed by a copper beryllium ion counting electron multiplier while ^4He was analysed by an electrically suppressed Faraday detector.

Determination of mass spectrometer sensitivity and mass discrimination was performed by measuring HESJ standard gas (Matsuda *et al.*, 2002) with $^3He/^4He = 20.63 \pm 0.10$ R_a. The average blank levels were $^3He = 1.7 \times 10^{-15} \pm 3.9 \times 10^{-17}$ cm^3, and $^4He = 1.7 \times 10^{-10} \pm 4.4 \times 10^{-11}$ cm^3. Repeated analysis of the HESJ standard revealed a reproducibility of 0.2 % and 1.1 % for ^4He and ^3He measurements,

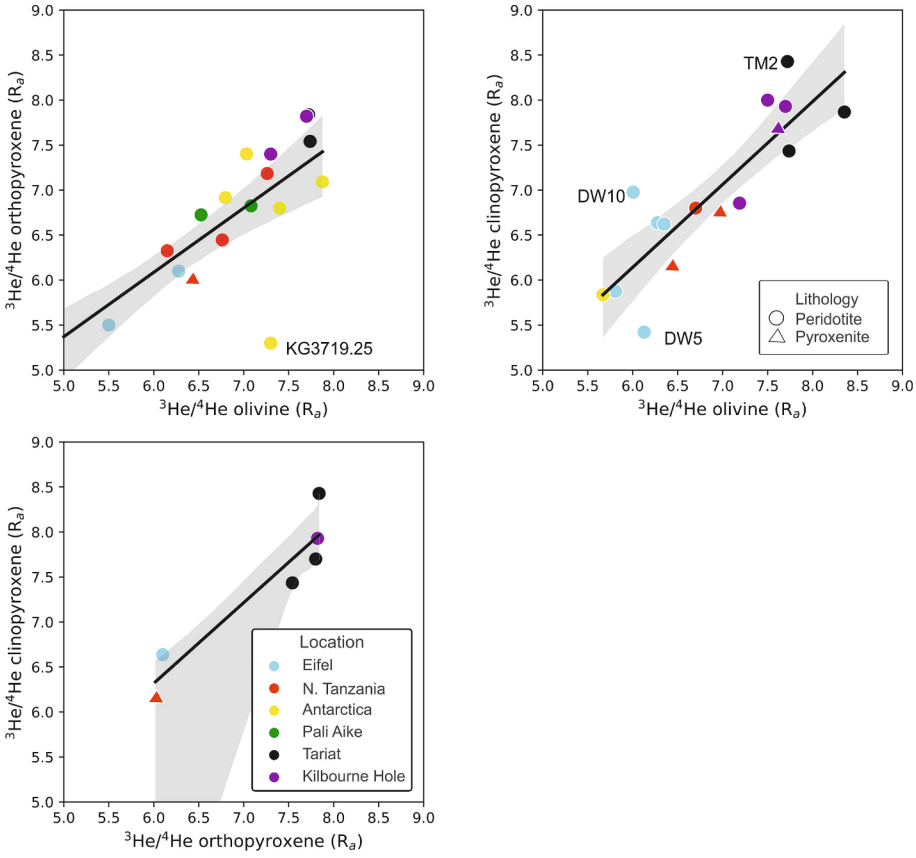

Fig. 2. Variations in ^3He and $^3He/^4He$ (normalised to atmosphere, where $R_a = 1.384 \times 10^{-6}$) of co-existing minerals separated from mantle xenoliths analysed in this study. Circles are peridotites and triangles are pyroxenites. The black solid line and shaded fields show the regression line through the data and confidence bands, respectively. Most xenoliths fall within these confidence bands. Data are from Table 1.

respectively. Helium concentrations were determined using the mass of material that passed through a 100 μm sieve after crushing.

$^3He/^4He$ and He concentration of xenoliths with multi-mineral analysis used a weighted average (see Supplementary Material). When more than one mineral from a single mantle xenolith was measured for $^3He/^4He$, the majority yielded correlations of that fall within the 1:1 confidence interval (Fig. 2). The exceptions are olivine in a sample from the Antarctic Peninsula (KG3719.25) that has less radiogenic $^3He/^4He$ than co-existing orthopyroxene, together with olivine and clinopyroxene in two samples from the Eifel (DW10 & DW5) and one from Tariat (TM2) which fall outside the 1:1 confidence interval on $^3He/^4He$ plots. This disequilibrium is more prevalent in the peridotites than the pyroxenites (Fig. 2 & Figure S7 in the Supplementary Material).

4. Results

4.1. Variations in He and $^3He/^4He$

The helium isotope and abundance data together with mineral chemistry and reconstructed whole-rock data are presented in Table 1

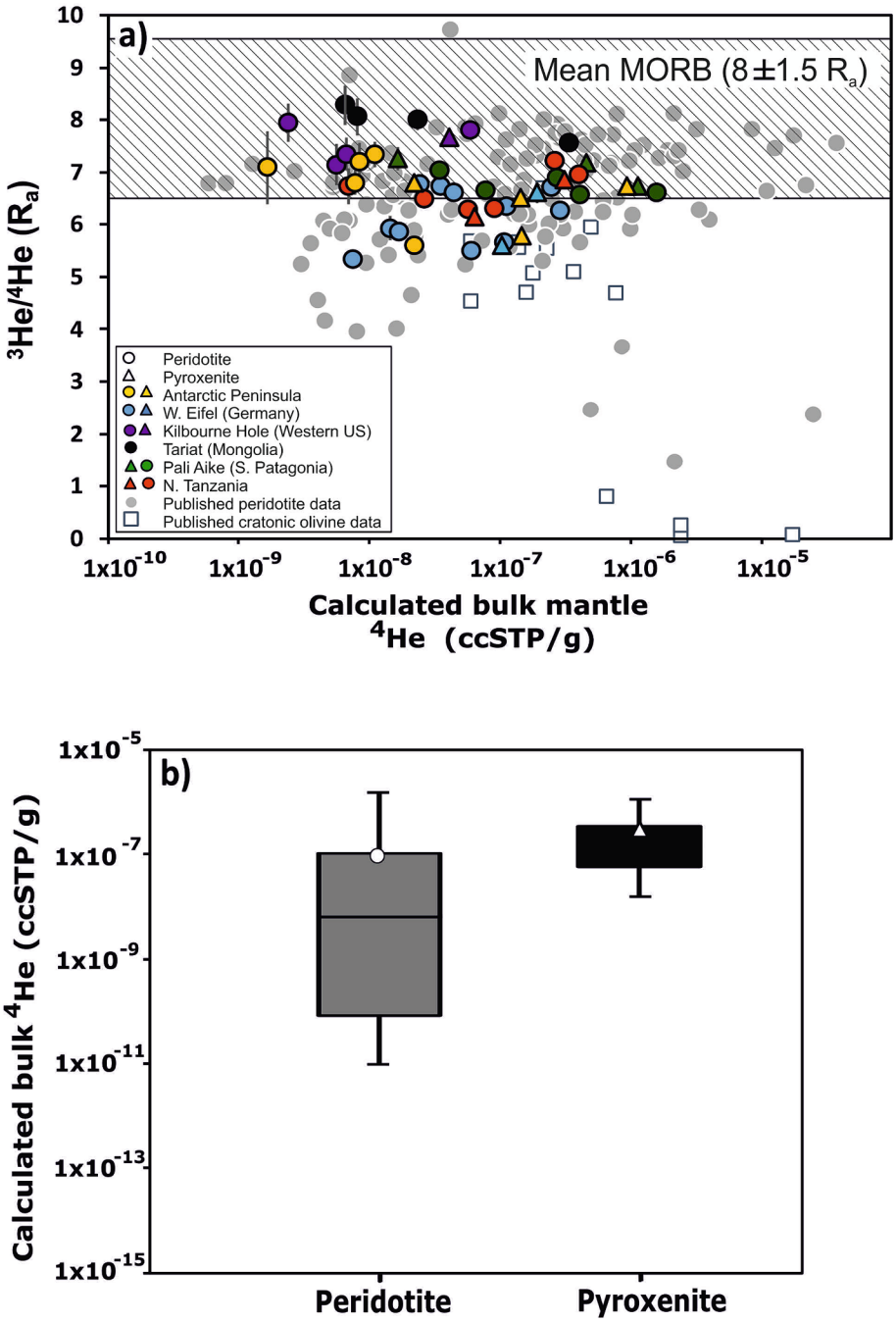

Fig. 3. (a) Co-variation of calculated bulk xenolith ^4He concentration and $^3He/^4He$ in on- and off-craton mantle xenoliths analysed in this study. Circles are bulk peridotites and triangles are bilk pyroxenites. The compositions of olivine in cratonic peridotites are shown for comparison (open squares). Grey field of modern MORB source mantle from Allègre et al. (1995). (b) Box and whisker plot illustrating variations in calculated bulk ^4He and ^3He concentrations of mantle peridotites and pyroxenites analysed in our study. Data are from this work (Supplementary File 4) and the published literature (Hoke et al., 2000; Gautheron et al., 2005; Kim et al., 2005; Sapienza et al., 2005; Martelli et al., 2011; Correale et al., 2012, 2019; Barry et al., 2015; Day et al., 2015, 2019; Sgualdo et al., 2015; Konrad et al., 2016; Berkesi et al., 2019; Kobayashi et al., 2019; Xu et al., 2019; Faccini et al., 2020; Barry and Broadley, 2021; Rizzo et al., 2021).

and the Supplementary Material. Concentrations of ^{3}He exhibit a wide range in mantle olivine and pyroxenes, varying from 9.1 × 10^{-15} to 1.5 × 10^{-11} cm^3/g at STP in the peridotites and 1 × 10^{-13} to 1.1 × 10^{-11} cm^3/g at STP in the pyroxenites (see Supplementary Material). The higher He concentrations in mineral phases from the pyroxenites are consistent with studies of other volatiles in mantle olivine and pyroxenes, and most likely reflect the typically volatile rich nature of pyroxenites (e.g., Gibson et al., 2020; Halldórsson et al., 2022).

The ^{3}He/^{4}He values of the mantle minerals analysed in our study range from 4.8 to 8.5 R_a (Table 1; Figs. 2 & 3a). These values overlap with the range previously reported for most lithosphere xenolith minerals (Matsumoto et al., 1997, 1998; Hoke et al., 2000; Gautheron and Moreira, 2002; Gautheron et al., 2005; Kim et al., 2005; Sapienza et al., 2005; Czuppon et al., 2009; Nardini et al., 2009; Beccaluva et al., 2011; Martelli et al., 2011; Correale et al., 2012, 2015, 2019; Halldórsson et al., 2014; Su et al., 2014; Barry et al., 2015; Day et al., 2015, 2019; Sgualdo et al., 2015; Konrad et al., 2016; Berkesi et al., 2019; Kobayashi et al., 2019; Xu et al., 2019; Faccini et al., 2020; Barry and Broadley, 2021; Rizzo et al., 2021). Since some of the xenoliths were collected from surface outcrops, it is possible that they contain *in situ* cosmogenic ^{3}He (Foeken et al., 2009). We adopted the same crushing procedure as Carrecedo et al. (2019) who showed by analysis of long-exposed spinel peridotite from Antarctica that < 0.1 % of the cosmogenic [He] in the crystal lattice was released. While this amount will vary from one mantle xenolith to another it is highly unlikely that significant cosmogenic ^{3}He is present. Fig. 3 also shows that no high ^{3}He/^{4}He samples have anomalously high ^{3}He concentrations ruling out a significant cosmogenic contribution in all of our samples. Calculated bulk mantle xenolith concentrations of ^{3}He range from 1.7 × 10^{-14} to 1.4 × 10^{-11} cm^3/g at STP, and for ^{4}He from 1.1 × 10^{-9} to 1.6 × 10^{-6} cm^3/g at STP (Fig. 3b), with higher concentrations typically found in the pyroxenites. The bulk ^{3}He/^{4}He of the peridotite and pyroxenite mantle xenoliths ranges from 5.3 to 8.1 R_a (Table 1). With the exception of the xenoliths from the Antarctic Peninsula there is no significant difference between ^{3}He/^{4}He for peridotites and pyroxenites at any given location.

4.2. Variations in major and trace elements

The Mg# (where Mg#=Mg/Mg + Fe × 100) of olivine, orthopyroxene and clinopyroxene in the garnet- and spinel-bearing peridotites from our study range from 89.4 to 92.0, 89.6 to 92.3, and 89.5 to 93.8, respectively (Table 1). The Al_2O_3 contents of the orthopyroxenes range from 1.1 to 4.9 wt% and are lowest in the garnet peridotites. The spinel grains exhibit a wide range in Cr_2O_3 (13.7 to 59.8 wt%) and Al_2O_3 (22.7 to 72.9 wt%), giving Cr# (where Cr#=(Cr/Cr + Al)) of 9 to 59. The most-depleted peridotites (i.e. those with high Mg# olivine and pyroxenes, low Al_2O_3 orthopyroxenes and high Cr# spinels) are typically from Lashaine (Tanzania) and West Eifel (Germany), while the xenoliths from Kilbourne Hole (western US) and Tariat (Mongolia) are the least-depleted (Table 1). Overall, mineral phases in the pyroxenites tend to be less enriched in FeO than the peridotites (e.g., orthopyroxene Mg# varies from 79.5 to 91.8 and olivine Mg# ranges from 78.4 to 88.4). Fig. 4 shows that scattered negative correlations exist between the Mg# of olivine and orthopyroxene and ^{3}He/^{4}He in the peridotites.

The whole-rock compositions of the mantle xenoliths were calculated by mass balance from mineral chemistry and modal mineralogy (see Supplementary Material). Bulk peridotite SiO_2 contents range from 42 to 47 wt% in the peridotites and pyroxenites. Bulk MgO in the peridotites and pyroxenites are more varied, ranging from 36 to 47 wt% and 16 to 31 wt%, respectively. FeO ranges from 6 to 9 wt% in the peridotites and 4 to 12 wt% in the pyroxenites, so that Mg# ranges from 89.2 to 92.4 and 72 to 91, respectively. Bulk CaO content also exhibits a wide variation from 0.25 to 6.5 wt% in the peridotites and 7 to 18.5 % in the pyroxenites. Likewise, Al_2O_3 ranges from 0.3 to 5 wt% in the peridotites and 1.5 to 23 wt% in the pyroxenites. In the xenoliths analysed in our study, some of the most magnesian and silica-rich but Ca-poor bulk compositions are from the only on-craton suite, i.e. Lashaine.

Clinopyroxene, amphibole and phlogopite are the main host of incompatible trace elements in mantle peridotites. In the peridotites from Tariat, Kilbourne Hole and Pali Aike the clinopyroxenes have normalised trace element patterns that are depleted in the most strongly incompatible trace elements. This contrasts with some clinopyroxenes from the W. Eifel (e.g. DW3, MM11, MM5, DW8, G18 & G17) and the Antarctic Peninsula (L7.201.1.41) that exhibit enrichments in Th and U relative to elements of similar compatibility (Figure S8). Enrichments in Th and U are also apparent in the amphiboles from West Eifel peridotite MM11.

The calculated bulk concentrations of incompatible trace elements exhibit large variations in mantle peridotites and pyroxenites. Figs. 5 & 6 show depleted mantle normalised patterns for the incompatible trace elements for off- and on-craton mantle together with their ^{3}He/^{4}He ratios. Peridotites from Tariat (Mongolia), Kilbourne Hole and Pali Aike (Patagonia) exhibit relatively flat normalised multi-element patterns and most elements are between 0.1 and 10 times those of the MORB source (Fig. 5a-c). For other continental off-craton locations the normalised multi-element patterns are more variable and are frequently enriched in Th and U relative to Nb and Ta, and often exhibit relative depletions at Zr and Hf, e.g., W. Eifel and the Antarctic Peninsula (Fig. 5d, g & h). The normalised multi-element patterns that we observe in our new dataset are comparable to those for samples previously analysed for helium isotopes and trace elements from Western Saudi Arabia (Konrad et al., 2016) and the Transylvania Basin (Faccini et al., 2020; Fig. 5e & f). The garnet peridotites from Lashaine are highly enriched in strongly incompatible trace elements (including Th and U) relative to those from the Kaapvaal craton (Premier Mine; McIntyre et al., 2021) and the reworked North China craton (Xu et al., 2019; Fig. 6). The peridotites from the reworked North China craton are distinguished by their variable concentrations of incompatible trace elements, e.g., Th, U, Pb, Zr and Hf.

Off-craton mantle xenoliths with bulk incompatible trace element signatures indicative of enrichment by small-fraction melts and fluids (i.e. with $[La/Yb]_n$ > 0.36 (DMM value)) have ^{3}He/^{4}He of 5 to 8 R_a (Fig. 5). Those with ^{3}He/^{4}He > 7 R_a include off-craton samples from the Antarctic Peninsula, Southern Patagonia, Yemen, Hyblean Plateau, Western Saudi Arabia, and the Southern Main Ethiopian Rift (this work, Halldórsson et al., 2014; Sgualdo et al., 2015; Konrad et al., 2016). Mantle xenoliths that show relative enrichments in incompatible trace elements, (especially Th and U) – and have more radiogenic ^{3}He/^{4}He (<7 R_a) – include off-craton xenoliths from the W. Eifel, the Antarctic Peninsula, NW Libya, and E. Transylvanian Basin (this work, Beccaluva et al., 2011; Rizzo et al., 2018, 2021; Faccini et al., 2020). In the Antarctic Peninsula xenolith suite, the peridotites have higher ^{3}He/^{4}He than the clinopyroxenites.

5. Origin of ^{3}He/^{4}He variability in the continental lithospheric mantle

The high ^{3}He/^{4}He of off-craton mantle peridotite xenoliths from Tariat (7.6–8.3 R_a) and Kilbourne Hole (7.1–7.9 R_a) slightly extend the range published for Kilbourne Hole (7.23–8.1 R_a; Day et al., 2015; Kobayashi et al., 2019); Yemen (7.2–7.9 R_a; Sgualdo et al., 2015), Western Saudi Arabia (6.8–7.7 R_a; (Konrad et al., 2016), the Kenya Rift (6.3–7.5 R_a; Halldórsson et al., 2014) and N.E. Australia (8.1–8.2 R_a; Czuppon et al., 2009). The lowest ^{3}He/^{4}He in our sample suite is recorded by the off-craton xenolith suites from the Antarctic Peninsula (5.6–7.3 R_a), Southern Patagonia (6.6–7.3 R_a) and the W. Eifel (5.3–6.8 R_a), with the Antarctic Peninsula and W. Eifel displaying a greater range than has been observed in many other off-craton mantle samples. We note that the W. Eifel samples with the lowest ^{3}He/^{4}He (G17 & G18) are amphibole bearing. Our samples from the Antarctic Peninsula extend to slightly more radiogenic ^{3}He/^{4}He than those determined for the West Antarctic Rift System (6.7–7.24 R_a) by Day et al. (2019). The W. Eifel

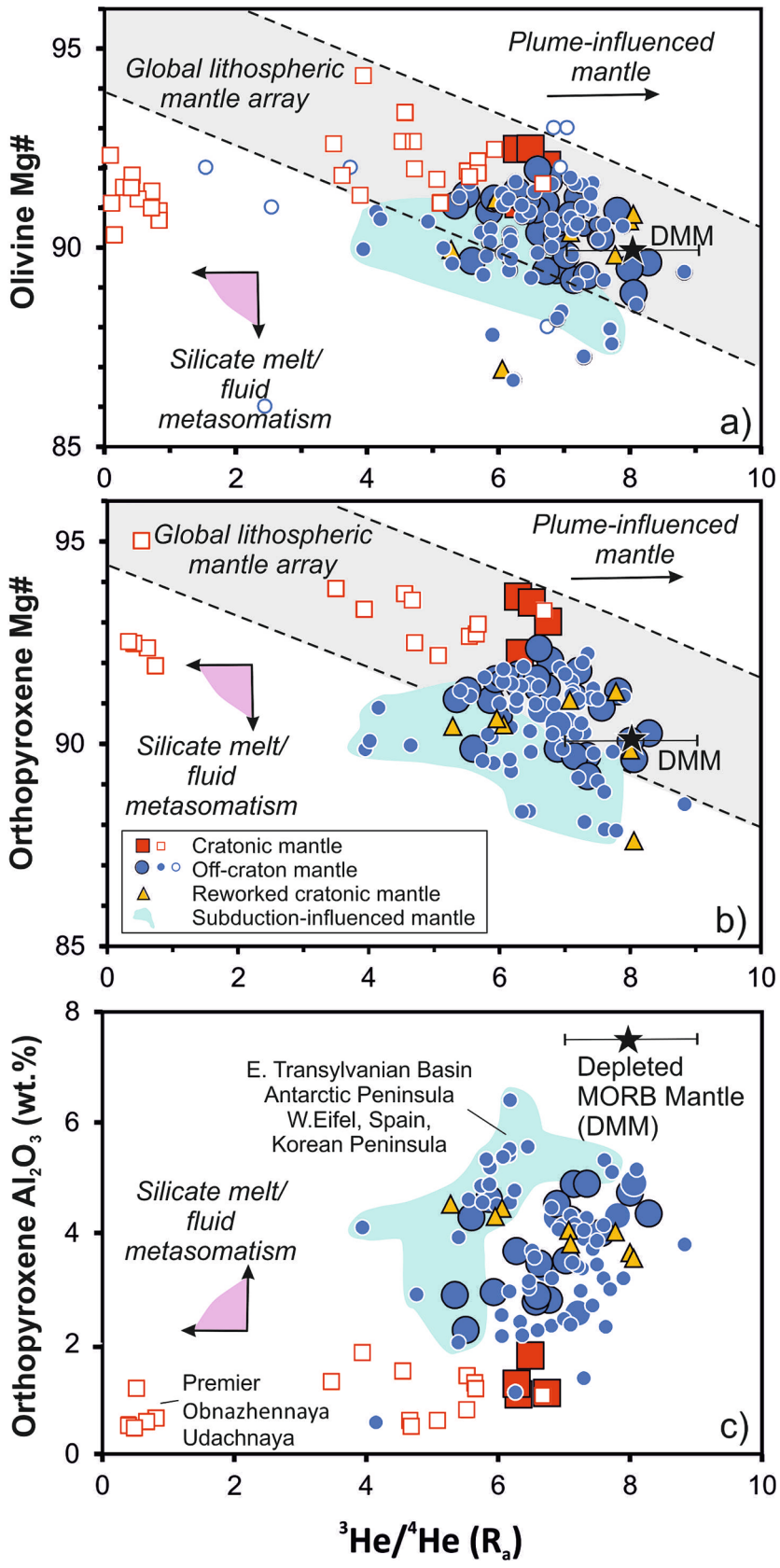

(caption on next page)

Fig. 4. $^3He/^4He$ versus: a) olivine Mg#; b) orthopyroxene Mg#; and c) orthopyroxene Al_2O_3 content. Solid symbols are for bulk xenolith $^3He/^4He$ and open squares are for $^3He/^4He$ in olivine or clinopyroxene. Open squares are off-craton xenoliths from the Dunedin Volcanic Field, New Zealand. Solid black star shows the composition of Depleted MORB-source mantle (DMM) based on the $^3He/^4He$ from Allègre et al. (1995) and olivine Mg# from Workman and Hart (2005). The lithospheric mantle array (shown by the grey shaded field) is inferred from the global continental peridotite database and excludes all peridotites that have undergone modal metasomatism (i.e. addition of amphibole and/or phlogopite) as a consequence of their interaction with subduction-related melts and fluids. Data from this work (large symbols) are from Supplementary File 4 and the published literature (Brandon and Draper, 1996; Dodson and Brandon, 1999; Hoke et al., 2000; Kim et al., 2005; Sapienza et al., 2005; Correale et al., 2012, 2019; Howarth et al., 2014; Barry et al., 2015; Day et al., 2015, 2019; Sgualdo et al., 2015; Konrad et al., 2016; Berkesi et al., 2019; Xu et al., 2019; Faccini et al., 2020; Rizzo et al., 2021).

xenoliths fall within the range previously observed for the European lithospheric mantle (6.1 ± 0.9 R_a; e.g., Dunai and Baur, 1995; Gautheron and Moreira, 2002; Rizzo et al., 2018, 2021; Faccini et al., 2020) and those for Southern Patagonia are similar to those analysed by Jalowitzki et al. (2016). The only on-craton mantle xenoliths that we analysed are from the rifted margin of the Tanzania craton (Lashaine). The $^3He/^4He$ of these xenoliths (6.2–6.7 R_a; Table 1) are at the high end of the range observed for on-craton mantle by Day et al. (2015; 0.5 – 6.7 R_a), and slightly higher than samples analysed from Lashaine by Halldórsson et al. (2014; 5.3–6.2 R_a). Below we discuss the causes of variations both within and between on- and off-craton mantle xenolith suites.

5.1. Lithological variability in the lithospheric mantle

During sub-solidus cooling of melt residues (primarily harzburgites) in the lithospheric mantle, the inclusions within the mantle phases (usually olivine and orthopyroxene) should retain the $^3He/^4He$of the convecting mantle, assuming that there is minimal $^3He/^4He$ fractionation during sub-solidus cooling (Trull and Kurz, 1993). In contrast, pyroxenites are typically found as veins and most likely represent the crystallisation products of the channellised flow of percolating convecting mantle derived melts (Wilshire et al., 1988). It is therefore likely that the $^3He/^4He$ of the pyroxenes and olivine in these veins were initially in equilibrium with the ascending convecting mantle-derived melts from which they precipitated.

5.2. Tectonic setting

Significant depletion experienced by ancient cratonic mantle is implicit from the chemistry of co-existing mineral phases. For example, the Mg# of olivines from refractory peridotite xenoliths (i.e. that have not been enriched by melt-rock reactions) are typically higher than those in off-craton mantle, with a threshold at ~92 (Fig. 7). Where mineral chemistry and reconstructed whole-rock data are available we observe a first order, negative relationship between the degree of melt depletion and $^3He/^4He$ of peridotite mantle xenoliths (Fig. 4). The xenoliths from cratonic settings with the most depleted major-element mineral compositions (i.e. harzburgites with high Mg# olivine and orthopyroxene, high Cr# spinel, and orthopyroxene with low Al_2O_3 content) have $^3He/^4He$ typically ranging from 3.5 to 7 R_a (Fig. 8). Exceptions to this are some of the cratonic xenoliths from the Siberian and Kaapvaal cratons that have low Mg# for a given $^3He/^4He$ (Fig. 4). The alkali basalt and basanite hosted peridotites from off-craton settings tend to have less depleted compositions, i.e. relatively low Mg# olivine and orthopyroxene (88–92.5), low Cr# spinel (<20) and high Al_2O_3 orthopyroxene contents (>2 wt%), and $^3He/^4He$ varying from 4.6 to 13.9 R_a (Figs. 4 and 8). This relationship is also evident from the calculated whole-rock major element compositions; the least-depleted peridotites (FeO>7 wt %) typically have higher $^3He/^4He$ (>7 R_a) than the more-depleted off-craton peridotites with FeO<7 wt% ($^3He/^4He$ = 5–7 R_a; Fig. 8a). We note that the xenoliths which plot off from the main global lithospheric mantle array on Fig. 4 have relatively low $^3He/^4He$ at given Mg# in olivine and orthopyroxene, and also orthopyroxene Al_2O_3 content. These include several off-craton peridotite xenoliths from Simcoe, Eastern Transylvanian Basin, Antarctic Peninsula, Korean Peninsula, Calatrava in Spain and W. Eifel (Brandon and Draper, 1996; Dodson and Brandon, 1999; Kim et al., 2005; Martelli et al., 2011; Faccini et al., 2020; Rizzo et al., 2021). Many of these off-craton peridotites contain amphibole (i.e. a hydrous, non-primary mantle phase) and are enriched in Th and U relative to elements of similar incompatibility (e.g. Nb; Fig. 5). They are located above past or present subduction zones —- e.g., the peridotites from the Antarctic Peninsula are hosted in Cenozoic (7.7–1.5 Ma) mafic alkaline volcanic rocks along the former Mesozoic to Early Cenozoic subduction margin of W. Antarctica and the W. Eifel mantle has been influenced by the Hercynian Orogeny (Lippolt, 1983; Leat et al., 2023) —- and may have interacted with silicic melts or C-O-H fluids derived from down-going slabs. In subducted slabs the noble gases are predominantly stored in amphibole and the most significant transfer will occur to the continental mantle immediately above this region, i.e. where the slab is at depths between ~80 and 100 km (Smye et al., 2017). Dodson and Brandon (1999) suggested that the proportion of sub-arc mantle with low $^3He/^4He$ may be small but the current global dataset implies that xenoliths with radiogenic $^3He/^4He$ are present in most xenolith suites associated with past convergent margins (Fig. 4).

Mantle peridotites from Udachnaya and Obnazhennaya (Siberia craton) and Premier (Kaapvaal craton) also plot off from the global lithospheric mantle array. Nevertheless, the measured $^3He/^4He$ for some of the cratonic mantle xenoliths emplaced at 1179 Ma at Premier and 360 to 160 Ma at Udachnaya and Obnazhennaya, respectively, may not reflect the original $^3He/^4He$. Some of the Udachnaya peridotites have extremely high ^4He that cannot be explained by radiogenic ingrowth alone (see below) and these are thought to contain slab derived fluids (Barry et al., 2015; Day et al., 2015).

5.3. Ingrowth of ^4He

The alpha decay of U and Th in mineral lattice generates ^4He. This *in situ* radiogenic He diffuses through the mineral lattice and a small proportion comes to rest in voids, such as cracks, fission tracks and inclusions. *In vacuo* crushing releases a small proportion of the *in situ* radiogenic He which will act to lower the $^3He/^4He$ of mantle peridotites. We have used the following equation to calculate the radiogenic ingrowth of ^4He:

$$\left[{}^4He\right] = 8\times\left(e^{\lambda 238t}-1\right)\times{}^{238}U + 7\times\frac{{}^{238}U}{137.88}\times\left(e^{\lambda 237t}-1\right) + 6\times\left(e^{\lambda 232t}-1\right)\times{}^{232}Th \quad (1)$$

where: [^{4}He] is 1x10^{-6} cm^3/g of ^{4}He at STP; t is time in billions of years; λ^{238}, λ^{237} and λ^{232} are the decay constants for ^{238}U, ^{237}U and ^{232}Th (0.155125, 0.00025, 0.049475 Ga^{-1}, respectively) and ^{238}U and ^{232}Th are the amounts present in ppm. We have also assumed that 0.1 % of lattice-bound ^4He is released by crushing. The effect of radiogenic ^4He release on $^3He/^4He$ for xenoliths from on– and off-craton locations with a range of Th and U concentrations are illustrated in Fig. 9. This figure shows the contribution of radiogenic ^4He on a depleted mantle peridotite from Tariat and a peridotite with high Th and U concentrations from the W. Eifel (DW8). The latter resembles peridotites interpreted as metasomatized by subduction fluids during the Hercynian Orogeny. The variations in the incompatible trace element patterns of the W. Eifel peridotites (Fig. 5g & h) suggests that there may have been variable amounts of overprinting by more recent metasomatic melts. Fig. 9 shows

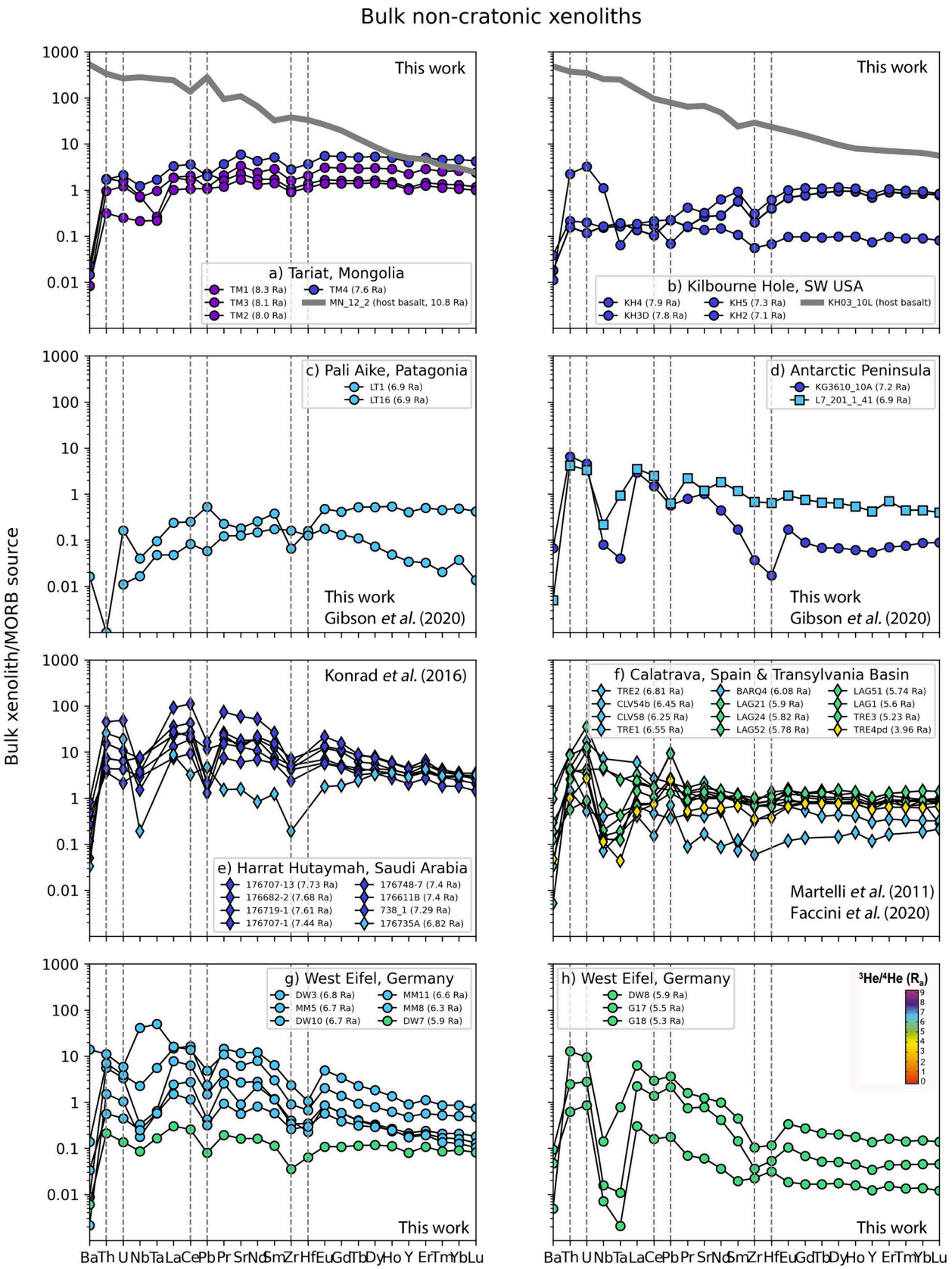

Fig. 5. Depleted-MORB-mantle-normalised incompatible-trace-element plots showing calculated bulk concentrations for off-craton continental peridotites analysed for $^{3}He/^{4}He$. Colour coding of symbols relates to $^{3}He/^{4}He$ ratio. Data sources are: this work (Supplementary materials); Martelli et al. (2022); Konrad et al. (2016); Faccini et al., (2020); Gibson et al. (2020). The compositions of corresponding host magmas are shown by solid grey lines for Tariat (Barry et al., 2007) and Kilbourne Hole (Harvey et al., 2012). Depleted mantle values are taken from Salters and Stracke (2004).

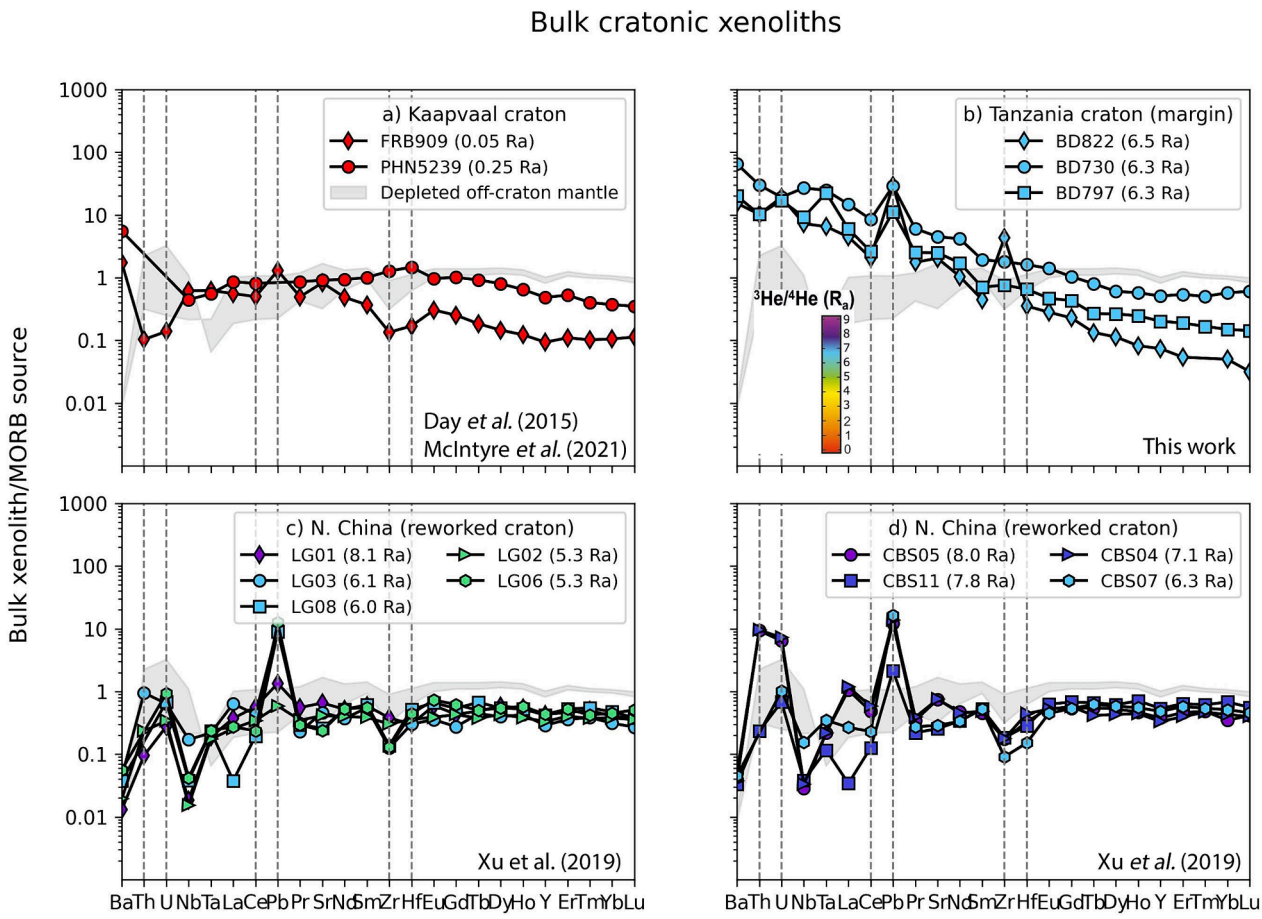

Fig. 6. Depleted-MORB-mantle-normalised incompatible-trace-element plots showing calculated bulk concentrations for cratonic peridotites analysed for $^{3}He/^{4}He$. Colour coding of symbols relates to $^{3}He/^{4}He$ ratio. The grey field for 'depleted off-craton peridotites' represents the analyses of samples from Tariat (TM2) and Kilbourne Hole (KH2) on Fig. 5. Data sources are: this work (Supplementary materials); Day et al. (2015); Xu et al. (2019); McIntyre et al. (2021). Depleted MORB mantle values are taken from Salters and Stracke (2004).

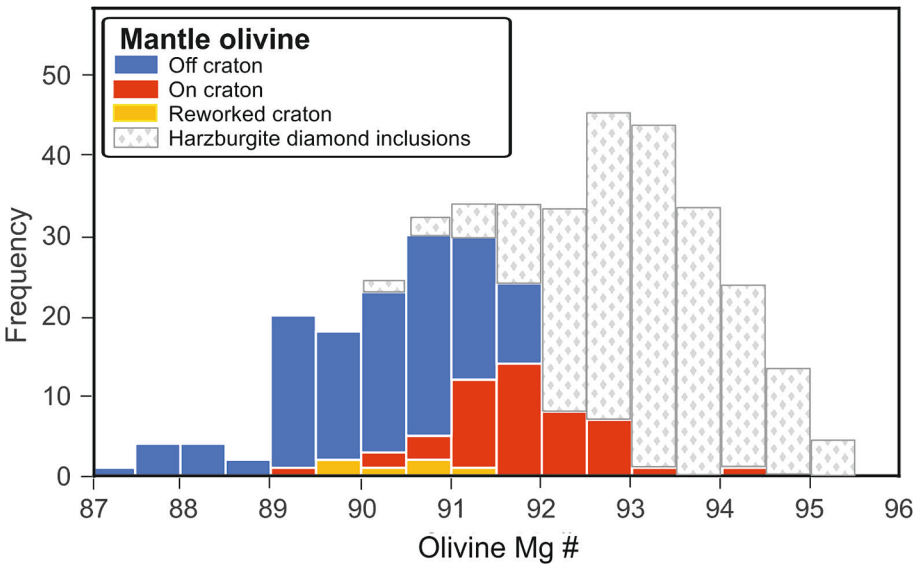

Fig. 7. Frequency density plot of the Mg# of olivines in mantle peridotites analysed for $^{3}He/^{4}He$ and inclusions in diamonds (Table 1 & Supplementary Materials; Brandon and Draper, 1996; Dodson and Brandon, 1999; Hoke et al., 2000; Kim et al., 2005; Sapienza et al., 2005; Stachel and Harris, 2008; Correale et al., 2012, 2019; Howarth et al., 2014; Barry et al., 2015; Day et al., 2015, 2019; Sgualdo et al., 2015; Konrad et al., 2016; Berkesi et al., 2019; Xu et al., 2019; Faccini et al., 2020; Rizzo et al., 2021).

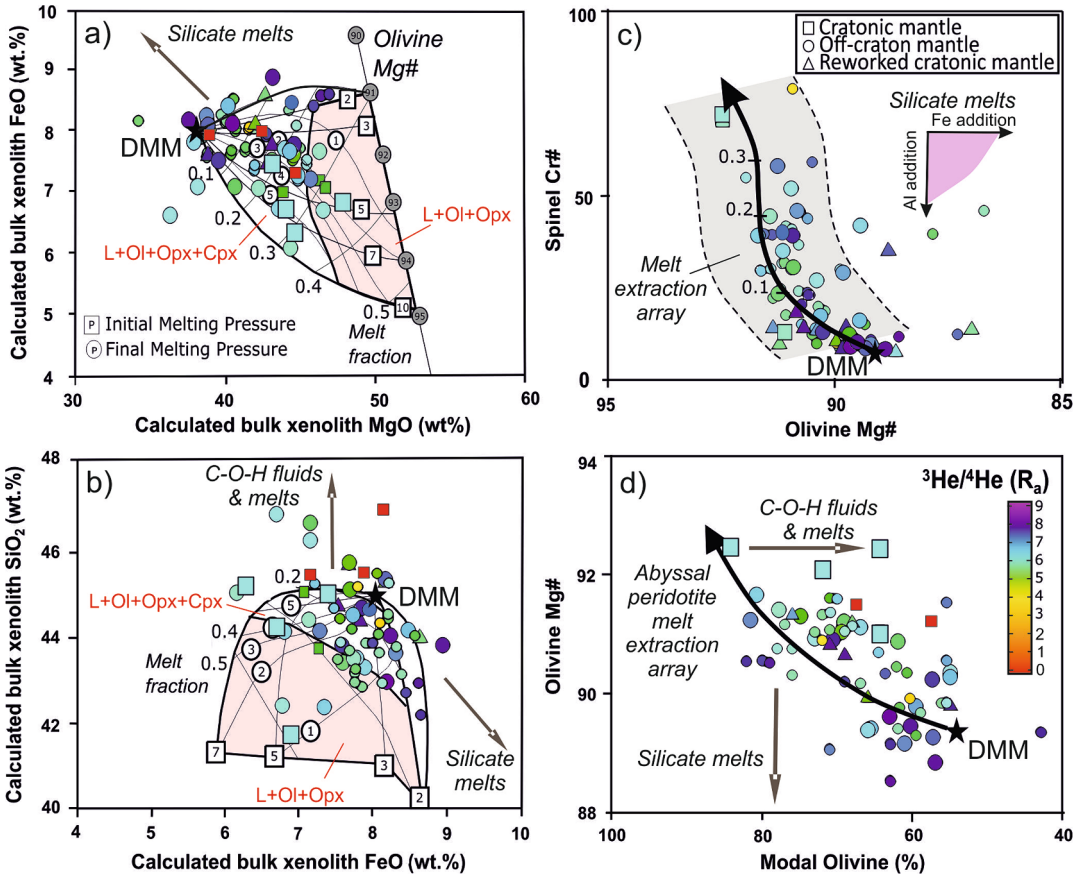

Fig. 8. Variation of calculated bulk xenolith $^3He/^4He$ with extent of melting and metasomatism in on- and off-craton mantle xenoliths. Variation in $^3He/^4He$ are shown together with: a) calculated bulk xenolith MgO and FeO; b) calculated bulk xenolith FeO and SiO_2; c) olivine Mg# and spinel Cr#; d) modal olivine and olivine Mg#. In plots (a) and (b) the melting model from Herzberg (2004) is included to illustrate the variation of $^3He/^4He$ with the pressure of adiabatic decompression melting, i.e. before the melt residues separated from the convecting mantle. Similarly, plots (c) & (d) show how $^3He/^4He$ varies with the melt-extraction arrays of Boyd (1989) and Arai (1994). In all plots the solid black star shows the composition of the Depleted MORB Mantle (DMM) source based on the $^3He/^4He$ from Allègre et al. (1995) and olivine Mg# from Workman and Hart (2005). FeO is calculated using the FeO:Fe_2O_3 method from Canil et al. (1994). Data are from this work (Supplementary Material) and the published literature (Martelli et al., 2011; Barry et al., 2015, 2015; Day et al., 2015; Sgualdo et al., 2015; Konrad et al., 2016; Correale et al., 2019; Xu et al., 2019; Faccini et al., 2020; Zhang et al., 2022).

that ^4He release is significant in samples that underwent ancient metasomatic enrichment and also those that were emplaced > 10 Ma = . The global lithospheric mantle array on Fig. 4 is therefore primarily inferred from the distribution of peridotite xenoliths that were entrained from continental lithospheric mantle < 10 Ma, and which has not been strongly influenced by ancient subduction-related fluids or melts.

5.4. Melt extraction

Off-craton mantle peridotites with the lowest incompatible trace-element enrichment resemble modern MORB source mantle including $^3He/^4He$ (7–9 R_a; Table 1 & Fig. 5). These characteristics are dominant in the mantle xenolith suites found distal to past and present subduction zones (e.g., Tariat (Mongolia), Kilbourne Hole (Western USA), Pali Aike (Patagonia)) and are common, albeit not ubiquitous, in Yemen and western Saudi Arabia xenolith suites (Sgualdo et al., 2015; Konrad et al., 2016). This is most easily explained by: (i) an ancient depletion event that has been overprinted by He derived from the host magma during entrainment; or (ii) recent underplating by asthenosphere mantle. The reconstructed bulk concentrations of strongly incompatible trace elements are lower than those in their host magmas (alkaline basalts; Fig. 6) and indicate limited melt-rock interaction during entrainment. The young Re-Os ages of peridotite xenoliths from both Tariat (Carlson and Ionov, 2019) and Kilbourne Hole (Harvey et al., 2011) indicate that parts of the underlying lithospheric mantle formed as the result of a 'young' melt extraction event, which tends to support the recent underplating model. Our interpretation of the $^3He/^4He$ determined in off-craton mantle xenoliths from Tariat and Kilbourne Hole is supported by the similarity of mineral and whole-rock chemistry of the xenoliths to depleted MORB mantle (see Section 4.1) and implies that thielithospheric mantle formed from modern-day upper-mantle. With the exception of the Red Sea rift zone and Afar (Halldórsson et al., 2014), there is no direct evidence for continental mantle peridotites entrained by < 100 Ma magmas having formed as a residue of melting in upwelling mantle plumes (i.e., $^3He/^4He$ > 10 R_a). This may be because the Red Sea rift zone and Afar represent a relatively unique tectonic setting, where a mantle plume is interacting with a major continental rift at a continent-ocean transition zone, and so atypical of the bulk continental mantle.

Fig. 8a & b show that off-craton mantle peridotites that plot in the field of melt residues formed of Ol + Opx + Cpx, and initially experienced < 25 % fractional melting in the convecting mantle at pressures < 4 GPa, typically have $^3He/^4He$ > 7 R_a (i.e. dark blue symbols). This relationship can be further scrutinised for spinel-bearing peridotites by examining the co-variation of $^3He/^4He$ with spinel Cr# and olivine Mg#. Peridotites with depleted spinel (Cr# >25) and olivine (Mg# >91) compositions, and that have experienced > 10 % melt extraction (Arai, 1994), have more radiogenic $^3He/^4He$ than those with less depleted mineral compositions (Fig. 8c). These observations are similar to the findings for the W. Eifel and Siebengebirge in Germany by Rizzo et al. (2021).

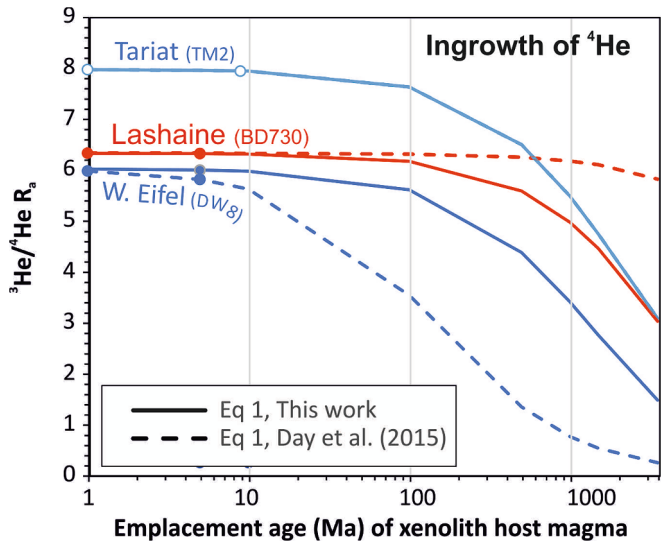

Fig. 9. The effects of ^{4}He ingrowth on ^{3}He/^{4}He with time for samples that have high and low concentrations of U and Th from off-craton settings (TM2 and DW8) and high U-Th from on-craton settings (BD730). Data are modelled using Equation (1) of this work and Equation (1) of Day et al. (2015). The closed circles show ages of emplacement of the host magmas. Sources for these are as follows: Eifel, ~0.5–0.01 Ma (Lippolt, 1983); Lashaine, Quaternary (Dawson, 2008) and Tariat, <6 Ma (Barry et al., 2003).

Conversely, mantle peridotites with compositions that reflect greater amounts of fractional melting (>25 %) at higher pressures usually record ^{3}He/^{4}He < 7 R$_a$. Some of the samples of cratonic mantle that have been analysed for ^{3}He/^{4}He fall in the L+Ol + Opx field on Fig. 8a & b and formed by up to ~ 35 % melting. Many of the other cratonic peridotites exhibit enrichments in SiO_2, FeO and orthopyroxene relative to experimental mantle melts (Fig. 8a, b, c & d) and so do not solely represent melt residues. These include the cratonic peridotites with the lowest ^{3}He/^{4}He ratios from the Premier Mine on the Kaapvaal craton (red symbols on Fig. 7).

5.5. Time-dependent melt extraction

By superimposing the calculated whole-rock composition of mantle peridotite xenoliths onto the fractional mantle melting models of Herzberg (2004) it is possible to interrogate the relationship between ^{3}He/^{4}He and the amount of melt-extraction. The degree of melt depletion recorded by mantle peridotites is primarily controlled by the temperature of the convecting mantle at the time of their initial formation as melt residues, and prior to their aggregation in the lithospheric mantle. The upper mantle is believed by many to have undergone secular cooling from the Archean when the mantle potential temperature (T_P) was ~ 1650 °C, to the present day when T_P is ~ 1330 °C (e.g., Richter, 1988). This has widely been attributed to be the cause of the difference in major element composition of ancient cratonic and younger off-craton continental mantle (e.g., Herzberg et al., 2010); peridotites with time-integrated model ages (i.e. from Re-Os and Lu-Hf isotopic systems) show a decrease in olivine Mg# from the Archean (Mg# = 94) to modern times (Mg# = 89.7; Servali and Korenaga, 2018). In the last 3.5 Ga the ^{3}He/^{4}He in the convecting mantle has likely evolved from 80 to 8 R$_a$ as a consequence of degassing and radiogenic He ingrowth (Porcelli and Elliott, 2008). Consequently, it is expected that the ^{3}He/^{4}He of on– and off-craton mantle should reflect formation age, i.e. older xenoliths should have higher values. However, this is not the case and it appears that the ^{3}He/^{4}He of older, more melt depleted peridotites are lower than younger off craton mantle. This can most easily be explained by the release of *in situ*-produced radiogenic He in the older xenoliths (Day et al., 2015).

To test whether the incorporation of radiogenic He in old lithospheric mantle explains the trends in Fig. 4 we have developed a model which integrates both the evolution of mantle ^{3}He/^{4}He (Porcelli and Elliott, 2008) and radiogenic helium ingrowth with temperature dependent melt-extraction models (Herzberg et al., 2010; Servali and Korenaga, 2018). This allows us to calculate the ^{3}He/^{4}He and olivine Mg# of the lithospheric mantle that formed between the Archean and the present-day. Our model assumes that mantle peridotite has 0.01 ppm ^{238}U and 0.13 ppm ^{232}Th (Table S3). These are the mean bulk concentrations from our new dataset and the published literature for samples analysed for ^{3}He/^{4}He. Due to the paucity of bulk U and Th data for cratonic peridotites analysed for ^{3}He/^{4}He, this value is biased towards the compositions of off-craton mantle. Based on the median ^{3}He content of peridotite xenoliths from this study, we have used an initial ^{3}He concentration in the continental mantle of 1×10^{-13} cm^3/g at STP. The ratio of heat generation to heat loss (i.e. the *Ur* ratio) is important because it controls the amount of melting and the Mg# of the melt and residue. We have elected to use a *Ur* ratio of 0.23 proposed for the convecting mantle (Herzberg and Rudnick, 2012), which is consistent with the geochemistry of the lithospheric mantle (see Supplementary Material & Pearson et al., 2021). The corresponding olivine Mg# for melt residues formed during the past 3.5 Ga is obtained from Servali and Korenaga (2018). The results of these calculations are shown in Table 2 and Fig. 9.

Our model shows that the more depleted 3.5 to 2.5 Ga cratonic mantle has evolved to lower ^{3}He/^{4}He than younger off-craton continental mantle (Fig. 10a & Table 2). Using the parameters from previous studies (Herzberg, 2004; Porcelli and Elliott, 2008; Herzberg et al., 2010; Servali and Korenaga, 2018), and assuming that the continental lithospheric mantle is a residue of melting of peridotite in the upper convecting mantle and has evolved as a closed system, our model predicts that samples of 2.5 to 3.5 Ga cratonic mantle containing olivine with Mg# = 93.2 to 94.5 should yield present-day ^{3}He/^{4}He of 2.9–3.7 R$_a$, while samples of < 2.5 Ga off-craton mantle with olivine Mg# = 89.7 to 93.2 should have ^{3}He/^{4}He ranging from 4.5 to 8 R$_a$ (Fig. 10b & Table 2). This closed system scenario provides the background variation of ^{3}He/^{4}He in melt residues with time. An assumption of both our work and previous studies is that the compositions of mantle xenoliths are representative of the continental mantle. Despite the uncertainties that arise from this assumption, the results of our calculations largely match the observed data from both our work and the published literature (Fig. 10b).

5.6. Metasomatism

Metasomatism by percolating small-fraction melts and fluids derived from MORB source mantle, subducted slabs or mantle plumes, is expected to overprint the fluid ^{3}He/^{4}He of the lithospheric mantle as well as modify the major and trace element composition (see Figs. 4, 5 & 6). The complexity of the processes involved makes this difficult to quantify although it will bias the data from the compositions of pure melt residues (e.g., Day et al., 2015). This is apparent in the Mg# of olivines in cratonic peridotite xenoliths with ^{3}He/^{4}He. Most have Mg# <93 whereas the Mg# of olivines found in harzburgitic diamond inclusions, i.e. largely unmetasomatised cratonic mantle, are between 92 and 96 (Stachel and Harris, 2008; Fig. 5). The overprinting of melt residue compositions is also clear from: (i) enrichments in silica relative to the predicted compositions of melt residues; and (ii) the high modal % of olivine at a given olivine Mg# in cratonic mantle xenoliths (Fig. 8). The low modal olivine is compensated for by excess orthopyroxene and commonly interpreted as silicate-enrichment associated with melts or fluids of subducted oceanic lithosphere (e.g., Kelemen et al., 1998; Bell et al., 2005). We note that the samples, which plot off the oceanic peridotite melt-extraction array of Boyd (1989; Fig. 8d), also record slightly lower ^{3}He/^{4}He (<7 R$_a$).

Recent work by Gibson and McKenzie (2023) has shown that

Table 2
Predicted evolution of $^3He/^4He$ (R_a) and olivine Mg# in mantle residues.

	Predicted evolution of $^3He/^4He$ (R_a) and olivine Mg# in mantle residues															
	3.5 Ga		3 Ga		2.5 Ga		2 Ga		1.5 Ga		1 Ga		0.5 Ga		0 Ga	
Age of formation (Ga)	$^3He/^4He$ (R_a)	Olivine Mg#	$^3He/^4He$ (R_a)	Olivine Mg#	$^3He/^4He$ (R_a)	Olivine Mg#	$^3He/^4He$ (R_a)	Olivine Mg#	$^3He/^4He$ (R_a)	Olivine Mg#	$^3He/^4He$ (R_a)	Olivine Mg#	$^3He/^4He$ (R_a)	Olivine Mg#	$^3He/^4He$ (R_a)	Olivine Mg#
3.5	81.40	94.00														
3	21.47	94.00	45.80	93.50												
2.5	12.08	94.00	17.95	93.50	28.80	93.20										
2	8.31	94.00	10.88	93.50	14.69	93.20	20.20	92.50								
1.5	6.27	94.00	7.72	93.50	9.59	93.20	12.16	92.50	14.30	91.75						
1	5.00	94.00	5.93	93.50	7.05	93.20	8.45	92.50	9.83	91.75	11.40	91.00				
0.5	4.12	94.00	4.78	93.50	5.53	93.20	6.41	92.50	7.25	91.75	8.42	91.00	9.70	90.50		
0	3.49	94.00	3.97	93.50	4.51	93.20	5.13	92.50	5.70	91.75	6.45	91.00	7.49	90.50	8.00	89.70

Estimates of olivine Mg# (Mg/Mg + Fe) in mantle residues are from Servali and Korenaga (2018), assuming a *Ur* of 0.23 (Herzberg and Rudnick, 2012). $^3He/^4He$ (R_a) are from Porcelli and Elliott (2008). The predicted $^3He/^4He$ (R_a) include ingrowth of ^4He estimated using Eq. (1). Assumes 0.01 % addition of ^4He to intrinsic ^4He in the fluid inclusions (see text for discussion).

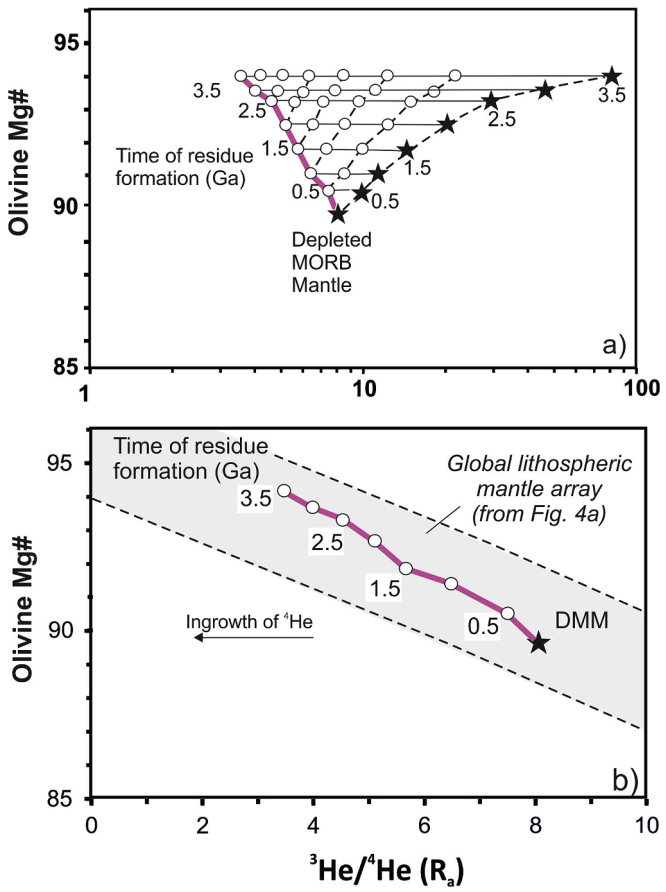

Fig. 10. (a) Time-dependent lithosphere evolution diagram comparing bulk xenolith $^3He/^4He$ with olivine Mg#. We follow Porcelli and Elliott (2008) and assume that $^3He/^4He$ at 3.5 Ga = 81.4 R_a, 3 Ga = 45.8 R_a, 2.5 Ga = 28.8 R_a, 2 Ga = 20.2 R_a, 1.5 Ga = 14.3 R_a, 1 Ga = 11.4 R_a, 0.5 Ga = 9.7 R_a, and 0 Ga = 8 R_a. Closed stars show the composition of the MORB source mantle at different time intervals and the closed circles show the estimated change in $^3He/^4He$ at 0.5 Ga time intervals. Details of parameters used in the model are presented in the main text. (b) Variation in olivine Mg# and bulk xenolith $^3He/^4He$ and the literature taken from Fig. 4a and overlain on the results of time-dependent lithosphere evolution models shown in (a). The global lithospheric mantle array and data are taken from Fig. 4. The solid curve shows the predicted present-day composition assuming 1.5 % addition of ingrown ^4He to intrinsic $^3He/^4He$ during crushing experiments (see Day et al., 2015).

addition of volatiles to cratonic mantle by metasomatic melts is balanced by loss through kimberlite and lamproite volcanism, and suggests this region has reached steady state. Less is known about off-craton mantle except that residence times will be shorter than for cratonic mantle and more work is required to improve constraints on the He fluxes. The extent to which the Mg# of the lithospheric mantle is influenced by metasomatism will vary according to the style of enrichment: high-Mg carbonate (dolomitic) melts may increase Mg# while silicate melts will decrease Mg#. Some of the deviations from the main global lithospheric mantle array shown in Fig. 4 may reflect this metasomatism. The off-craton Zealandia peridotites (East Otago & Chatham Island) which have highly variable $^3He/^4He$ and moderately high Mg# (Hoke et al., 2000) are thought to represent fragments of oceanic mantle swept into the Gondwana sub-arc environment and variably re-melted to generate the refractory residues (Scott et al., 2019). Metasomatism may also account for some of the cratonic mantle peridotites that fall off the global array, including those from the Kaapvaal craton (Premier Mine) and Siberia craton which have variable $^3He/^4He$ (0.1–5.6 R_a) but relatively low Mg# olivine and orthopyroxene (Fig. 4), and appear to have undergone modification by subduction-related fluids (Barry et al., 2015;

Day et al., 2015; Barry and Broadley, 2021; Zhang et al., 2022). The peridotites from the eastern margin of the Tanzania craton (Lashaine) fall within the main global lithospheric mantle array but have relatively low olivine Mg# (91–92.5) and high $^3He/^4He$ (6.3–6.7 R_a) compared to other on-craton xenoliths. Although this xenolith suite retains Archean Re-Os sulfide ages (up to 3 Ga; Burton et al., 2000), the peridotites are highly enriched in strongly incompatible trace elements (Fig. 6). This metasomatic signature is present in the Lashaine samples that we analysed for $^3He/^4He$ and consistent with interpretations from their incompatible trace element, Sr, Nd Pb and Os isotopic ratios which indicate a Proterozoic to Recent metasomatic enrichment (e.g., Cohen et al., 1984; Burton et al., 2000; Gibson et al., 2013).

The correlations outlined above imply that the $^3He/^4He$ trapped in fluid inclusions in continental lithospheric mantle phases are affected by subsequent events. This is consistent with the abundant evidence which shows that metasomatism of the lithospheric mantle has overprinted many of the initial depleted major and incompatible trace element and isotopic signatures (e.g., Menzies, 1983; Dawson, 1984). To resolve the cause of the local variations in the $^3He/^4He$ of continental mantle, we investigate relationships of $^3He/^4He$ with signatures indicative of: (i) different metasomatic agents, i.e. carbonatite and silicate melts or fluids; and (ii) melts or fluids derived from different reservoirs, e.g., subducted oceanic crust and the MORB source mantle (due to the absence of $^3He/^4He > 10$ R_a in data sets with incompatible trace elements concentrations we do not consider the deep mantle). In this work, we have concentrated on the light and heavy rare-earth elements (LREE and HREE) together with large-ion-lithophile elements (LILE) in bulk xenoliths (see Supplementary Material) because of their: (i) different behaviour during melting of the convecting mantle and subducted oceanic lithosphere; and (ii) large variations in mantle xenolith suites (Fig. 11a & b). The LREE/HREE ratio is tracked by $[La/Yb]_n$ (normalised to Depleted MORB Mantle after Salters and Stracke, 2004), which has a large range (0.3 to 90). Ratios of LILE and HREE are tracked by $[Th/Yb]_n$, which also varies widely (0.1 to 205). Incompatible trace element ratios such as $[Ti/Eu]_n$ and $[La/Yb]_n$ of clinopyroxenes are widely used to distinguish between silicate and carbonatite metasomatic agents (Coltorti et al., 1999) but Fig. 11 shows that while the variability in these trace element ratios may be due to different metasomatic agents there is no systematic variation of either of these ratios with $^3He/^4He$. This may be because enrichment of the lithospheric mantle from silicate or carbonatitic melts is complex and can increase or decrease $^3He/^4He$ depending on the age and source of the metasomatic melts and the age of the lithospheric mantle with which they are interacting.

Our work shows that off-craton mantle xenoliths with $^3He/^4He > 7$ R_a tend to resemble MORB source mantle, whereas those with lower $^3He/^4He$ (<7 R_a) are dominated by higher $[La/Yb]_n$ and $[Th/Yb]_n$ than MORB source mantle (Fig. 5) and contain clinopyroxenes with intermediate $[Ti/Eu]_n$ (0.1–1, Fig. 11c). These characteristics are typical of melts and fluids from subducted oceanic lithosphere (e.g. Kessel et al., 2005). While this interpretation favours the input of recycled material, the more radiogenic $^3He/^4He$ and high LILE/HREE might also reflect an ancient metasomatic event that became isolated and underwent ^4He ingrowth. We also cannot rule out the contribution of metasomatic melts derived from 'streaks' of ancient enriched (pyroxenite) material in the convecting upper mantle. These would have elevated U and Th relative to those from the surrounding upper mantle. In this case ingrowth of ^4He would be faster than depleted peridotites and typically generate lower $^3He/^4He$. Variations of $^3He/^4He$ with major and trace elements displayed in Fig. 11d reflect these different mechanisms and show that many of the peridotites with elevated LILE/HREE and lower $^3He/^4He$ also have a depleted chemistry (e.g., olivine Mg# >92), consistent with ancient lithosphere formation and substantial ^4He-ingrowth.

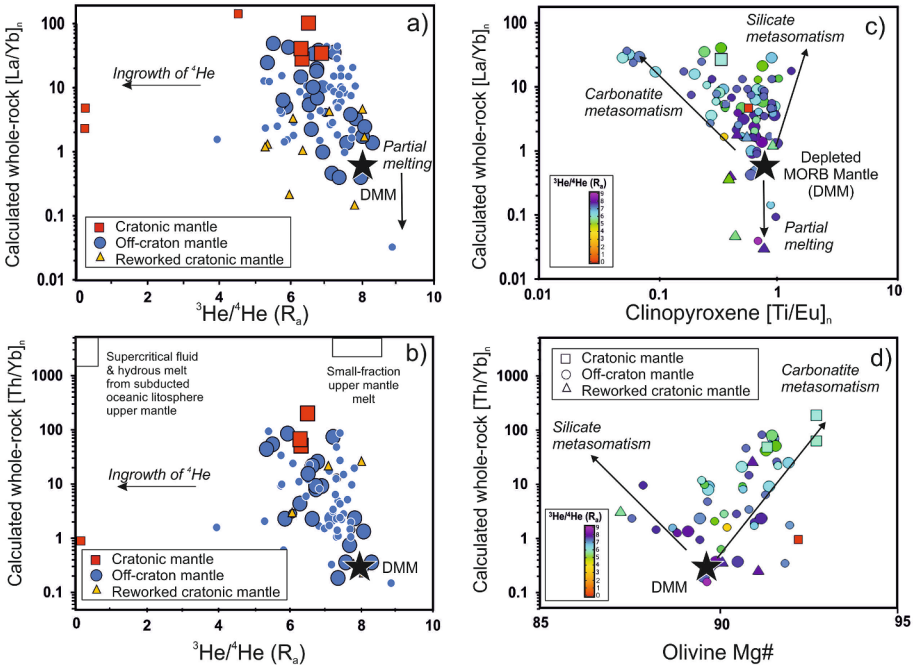

Fig. 11. Variation of $^3He/^4He$ with different indices of metasomatism in mantle peridotites. Note that only a few samples of cratonic mantle with $^3He/^4He$ have corresponding trace element analyses. (a) and (b) show calculated bulk xenolith $^3He/^4He$ vs $[La/Yb]_n$ and $Th/Yb]_n$, respectively, where $_N$ denotes normalisation to Depleted MORB Mantle (Salters and Stracke, 2004). The compositions of supercritical fluids derived from subducted oceanic lithosphere (Kessel et al., 2005), hydrous melt from recycled oceanic lithosphere (Hermann and Rubatto, 2009) and small-fraction upper-mantle melt (Blundy and Dalton, 2000) are shown for reference. Panel (c) illustrates the variations in clinopyroxene $^3He/^4He$ with $[Ti/Eu]_n$ and $[La/Yb]_n$ and (d) shows the variation in olivine Mg# and calculated bulk xenolith $[Th/Yb]_n$, both panels are colour coded for $^3He/^4He$. On all panels, the solid black star represents Depleted MORB Mantle (DMM; Salters and Stracke, 2004; Workman and Hart, 2005). Field of modern MORB Source mantle is from Allègre et al. (1995). Data are from this work (Supplementary Files 2 & 4) and the published literature (Martelli et al., 2011; Barry et al., 2015; Sgualdo et al., 2015; Konrad et al., 2016; Correale et al., 2019; Xu et al., 2019; Faccini et al., 2020; Gibson et al., 2020; McIntyre et al., 2021; Zhang et al., 2022).

Importantly, the effects of the metasomatic melts do not appear to be the primary control of the long wave-length variability of $^{3}He/^{4}He$ with Mg# in on– and off-craton continental mantle but more $^{3}He/^{4}He$ data is required for fully-characterised mantle xenoliths (i.e. modal mineralogy, major and trace element mineral chemistry) in order to statistically interrogate the effects of mantle metasomatism. These internally consistent datasets are especially sparse for the cratonic mantle.

6. Broader implications

Continental intraplate magmas exhibit wide variations in $^{3}He/^{4}He$ ratios (e.g., Stuart et al., 2003; Day et al., 2005; Horton et al., 2023). The highest $^{3}He/^{4}He$ (up to 67.2 R_a) are found in proto-Iceland plume picritic magmas from Baffin Island (Horton et al., 2023); these are believed to be a consequence of adiabatic decompression melting of entrained mantle plume material that contained helium diffused from the core (e.g. Starkey et al., 2009). Most other continental mafic magmas are more radiogenic ($^{3}He/^{4}He$ < 15 R_a) and may reflect melting of degassed plume mantle, MORB source mantle and assimilation of continental lithosphere (e.g., Reid and Graham, 1996; Dodson et al., 1998; Barfod et al., 1999; Kurz and Geist, 1999; Hoke et al., 2000; Day et al., 2005, 2023; Hilton et al., 2011). It has been argued that crustal assimilation only causes small variations in the $^{3}He/^{4}He$ of small volume continental magmas – due to their short residence times in the crust (Dodson et al., 1998) and that olivine typically forms, and therefore trap melt/volatile-rich inclusions, prior to crustal contamination (Stuart et al., 2000). The wide range in $^{3}He/^{4}He$ of fluid inclusions trapped in lithospheric mantle phases and the distinct signatures of on– and continental off-craton mantle (this work & Day et al., 2015) indicate that the $^{3}He/^{4}He$ of the continental lithospheric mantle is considerably more variable than earlier studies have suggested (e.g., Gautheron and Moreira, 2002).

Our confirmation that $^{3}He/^{4}He$ in mantle xenoliths differ between on and off-craton settings (see Day et al., 2015) and also subduction zones has broader implications for the variability of $^{3}He/^{4}He$ in magmas. Some CO_2-rich, silica-undersaturated continental mafic alkaline intraplate magmas (melilitites and nephelinites) have $^{3}He/^{4}He$ as low as 3 R_a, which may reflect their derivation from carbonated peridotite in the lower lithosphere (Day et al., 2023). These magmas are derived from shallower depths than kimberlites (Pintér et al., 2021) and lack the large cargo of lithospheric mantle olivine (typically 20–30 vol% or more) that is characteristic of kimberlites (Dawson, 1980). The ascent of proto-kimberlites through thick ancient mantle is fuelled by the preferential digestion of orthopyroxene from entrained wall-rocks; this decreases melt MgO content and drives exsolution of CO_2 (Russell et al., 2012). Since olivine and orthopyroxene from ancient cratonic mantle are characterised by radiogenic $^{3}He/^{4}He$ (this work; Day et al., 2015) and $^{143}Nd/^{144}Nd$ (e.g., Pearson and Wittig, 2014), the entrainment of olivine and dissolution of a large amount of orthopyroxene during kimberlite ascent (approximately 20–30 %; Russell et al., 2012) will dramatically decrease the melt $^{3}He/^{4}He$ and $^{143}Nd/^{144}Nd$ (Fig. 12). Mantle orthopyroxene and phlogopite will have lower Mg/Si than olivine and the final bulk Mg/Si of the kimberlite will be dependent upon the extent to which these different phases are entrained and digested. Olivine that subsequently crystallises from the kimberlite melt will have relatively low $^{3}He/^{4}He$, Mg# and $^{143}Nd/^{144}Nd$. This is supported by the limited

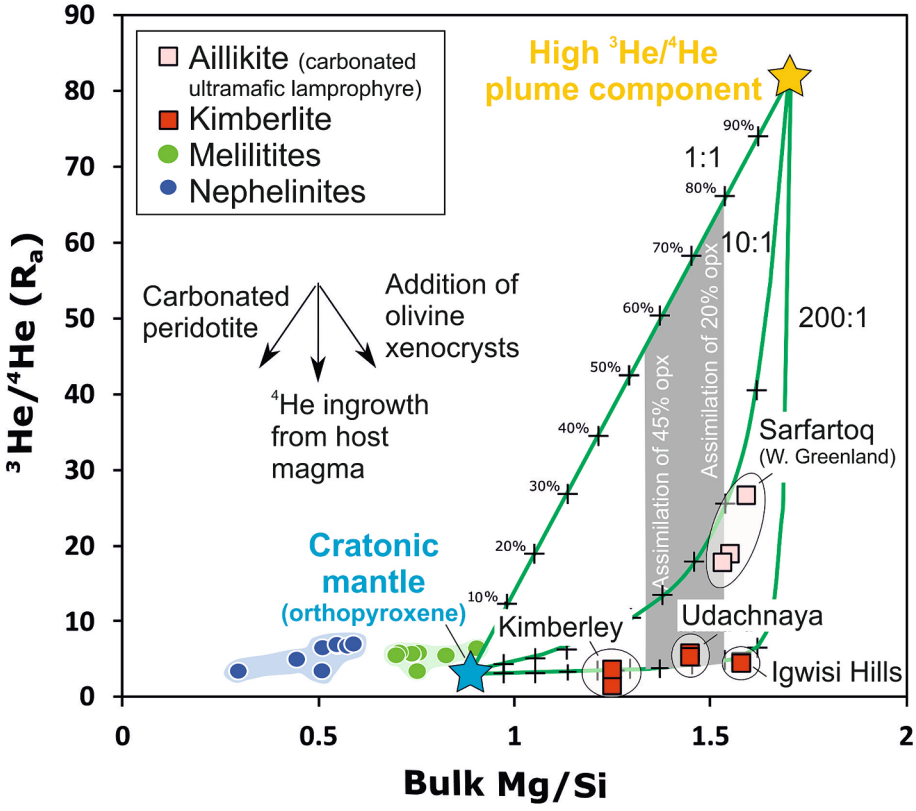

Fig. 12. Binary mixing models (after Langmuir et al., 1978) illustrating the effects of assimilation of cratonic mantle with proto-kimberlite melts on bulk $^{3}He/^{4}He$ and Mg/Si. The $^{3}He/^{4}He$ of cratonic mantle orthopyroxene and proto-kimberlite melt end member were assumed to be 2.89 and 82, respectively (Porcelli and Elliott, 2008; Day et al., 2015). Bulk Mg/Si ratios were assumed to be 0.87 and 1.7 for the cratonic mantle orthopyroxene and proto-kimberlite melt, respectively (Giuliani et al., 2020a; Jackson and Gibson, 2023). In the assimilation models Mg/Si was fixed at 1:1 but $^{3}He/^{4}He$ was varied as shown by the ratios adjacent to the curves. Data sources for kimberlites and aillikites are as follows: Udachnaya (Sumino et al., 2006); Kimberley (Giuliani et al., 2020b); Igwisi Hills (Brown et al., 2012; Willcox et al., 2015); West & South Greenland (Tachibana et al., 2006; Gaffney et al., 2007). The data for nephelinites and melilitites are from Day et al. (2005 and 2023) and Janney et al. (2002).

$^3He/^4He$ analyses that are available for fluid inclusions in kimberlite olivines (1.6–4.6 R_a; Brown et al. 2012; Giuliani et al., 2020b). We therefore propose that in many cases the incorporation of olivine and assimilation of orthopyroxene from the cratonic mantle most likely accounts for the rarity of kimberlite olivines (xenocrysts or phenocrysts) with high $^3He/^4He$ in certain locations (Fig. 12).

Olivines with relatively unradiogenic $^3He/^4He$ (up to 26.2 R_a; Tachibana et al., 2006; Gaffney et al., 2007) are found in CO_2-rich, high-MgO magmas known as aillikites; Tappe et al., 2011). These carbonated ultramafic lamprophyres were emplaced as dykes at Sarfartoq in West Greenland, on the northern margin of the North Atlantic craton. The olivines analysed by Tachibana et al. (2006) are small (0.5 mm to 1 mm) and given their unradiogenic $^3He/^4He$ appear to have crystallised directly from the aillikite melt. Importantly, the West Greenland aillikites have higher bulk-rock Mg/Si ratios (1.53; Gaffney et al., 2007) than global kimberlites (1.31 ± 0.16; Giuliani et al., 2020b) which suggests that the parental melts ascended through the lithospheric mantle without assimilating large amounts of mantle material (Fig. 12). Notably, the lithospheric mantle beneath the North Atlantic craton has less excess orthopyroxene than other cratons (Bernstein et al., 2007) and so the $^3He/^4He$ of melts traversing through this region are less susceptible to overprinting by dissolution. More work is required, however, to determine the full extent of the variability of $^3He/^4He$ in well-characterised kimberlites and associated high MgO magmas (lamproites and ultramafic lamprophyres), including the analysis of fresh olivine phenocrysts (as opposed to xenocrysts). This would place improved constraints on the He-concentrations in the cratonic mantle and proto-kimberlites (shown by 1:1 to 1:100 mixing lines on Fig. 11) and the role of ^4He-ingrowth from the host-kimberlite.

An additional broader implication from our study is that helium is typically more concentrated in mantle minerals found in pyroxenites than in peridotites. This observation expands the dominance of pyroxenites to be the major mantle repository for lattice-hosted volatiles, such as H_2O and F (Gibson et al., 2020) and CO_2 (Halldórsson et al., 2022) to also include fluid-hosted He. Despite their high concentrations of volatiles, pyroxenites form a relatively small proportion of continental mantle and do not significantly affect budgets of CO_2, He etc. They are, however, relatively fusible and easily mobilised during heating and

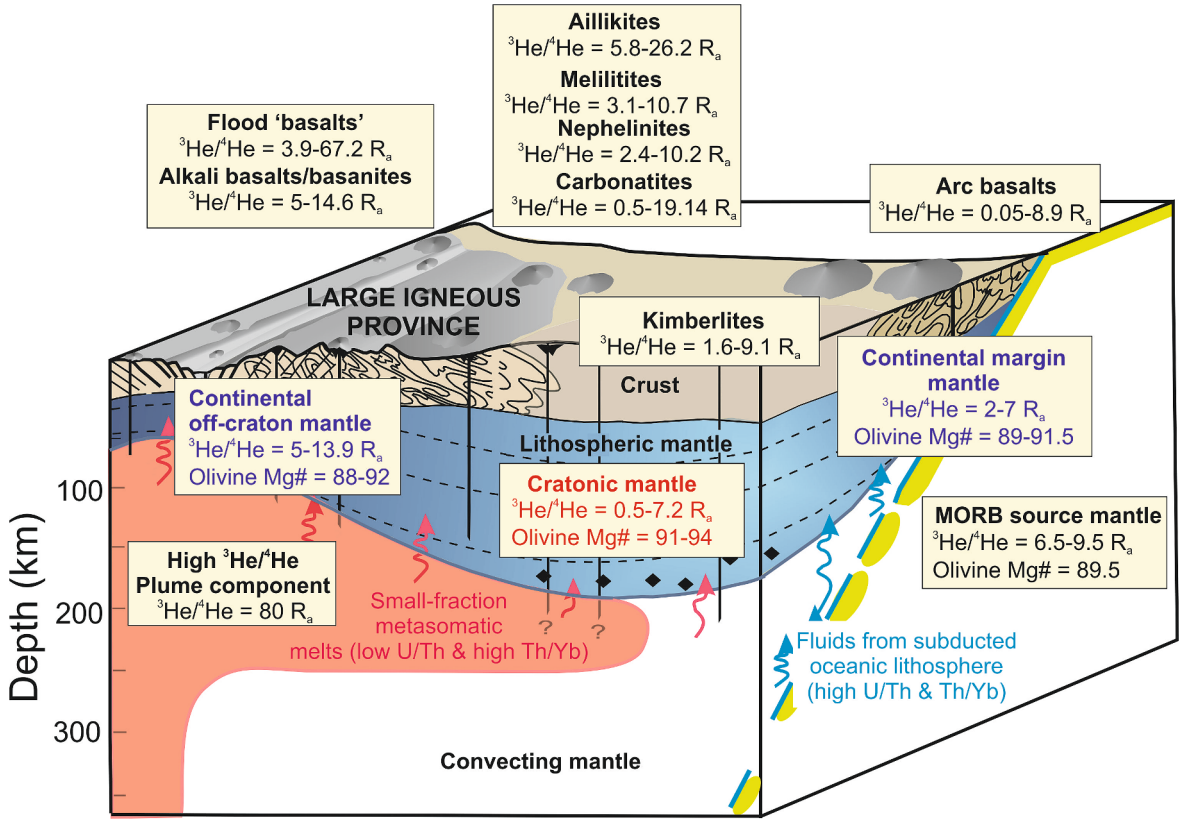

Fig. 13. Summary diagram showing variations in $^3He/^4He$ of the lithospheric mantle at different tectonic settings, based on data from mantle xenoliths presented. The $^3He/^4He$ of various reservoirs in the convecting mantle are shown for comparison. Our work confirms that the overall global trend of $^3He/^4He$ in the continental lithospheric mantle is governed by the age of the lithosphere (Day et al., 2015) and the amount of melting involved in its initial formation as a residue in the convecting mantle. Superimposed on this time-dependent global melt extraction array are the effects of metasomatism, which can be identified from major and incompatible trace element concentrations. For example, the lithospheric mantle beneath both cratons and continental margins is characterised by radiogenic $^3He/^4He$ but the former is more refractory, e.g., has olivine with higher Mg# (where Mg#= Mg/(Mg + Fe)). Continental off-craton mantle has similar $^3He/^4He$ to MORB except: (i) where it has been enriched by melts or fluids from subducted oceanic lithosphere (e.g., Faccini et al., 2020) and $^3He/^4He$ is lower, or (ii) is underlain by a mantle plume and $^3He/^4He$ is higher, e.g., the Red Sea and Afar (Halldórsson et al., 2014). The main data sources are as follows: cratonic mantle; this work, Day et al. (2015), Barry et al. (2015); Barry and Broadley (2021); continental off-craton mantle, this work, Gautheron and Moreira (2002), Czuppon et al. (2009), Beccaluva et al. (2011), Halldórsson et al. (2014), Sgualdo et al. (2015), Jalowitzki et al. (2016), Konrad et al. (2016), Rizzo et al. (2018, 2021); continental margin mantle, Brandon and Draper (1996), Dodson and Brandon (1999), Hoke et al. (2000), Kim et al. (2005), Martelli et al. (2011), Correale et al. (2012 and 2019), Day et al. (2019), Faccini et al. (2020); high $^3He/^4He$ plume component, Porcelli and Elliot (2008); MORB source mantle, Graham (2002); Hilton et al. (2002); kimberlites, Sumino et al. (2006), Tachibana et al. (2006), Brown et al. (2012); aillikites, Tachibana et al. (2006); melilitites, Day et al. (2005 and 2023); carbonatites, Marty et al. (1998), Tolstikhin et al. (2002); flood basalts, Stuart et al. (2003), Heinonen and Kurz (2015), Horton et al. (2023); alkali basalts/basanites, Barfod et al. (1999), Halldórsson et al. (2014), Day et al. (2023); volcanic arcs, Hilton et al. (2002) (For interpretation of the references to colour in this figure legend, the reader is referred to the web version of this article.)

.

rifting events (Gibson et al., 2020).

7. Conclusions

Our new analyses of mantle xenoliths from both on-craton (e.g., N. Tanzania) and 'off-craton' locations (e.g., West Eifel, Kilbourne Hole, Tariat and Antarctic Peninsula) reveal that co-existing minerals in peridotite and pyroxenite mantle xenoliths have similar $^3He/^4He$ and ^3He- and ^4He-concentrations. This observation differs from Dunai and Porcelli (2002) who reported higher ^4He-concentrations in pyroxenes. This may be because our study used a crushing procedure (rather than the laser-heating procedure of Dunai and Porcelli, 2002), which minimises the amount of He released from crystal lattices and where ^4He may preferentially accumulate by recoil processes from U+Th decay.

We have observed systematic differences within the $^3He/^4He$ of off-craton mantle and also between on– and off-craton mantle (Fig. 13). The $^3He/^4He$ of off-craton mantle varies, with some locations exclusively retaining $^3He/^4He$ signatures > 7 Ra (e.g., Kilbourne Hole, western US and Tariat, Mongolia), others have more radiogenic signatures < 7 Ra (e.g., W. Eifel, Germany), and the remainder preserve a wide range of $^3He/^4He$ (e.g., Antarctic Peninsula). The elevated $^3He/^4He$ of off-craton peridotites (8.2–10.4 R_a) and pyroxenites (12.7–13.9 R_a) from the Red Sea rift zone and Afar (Halldórsson et al., 2014) represent the relatively unique interaction of a mantle plume with a major continental rift at a continent-ocean transition zone, and atypical of continental off-craton mantle. Importantly, the $^3He/^4He$ signatures of off-craton mantle xenoliths are more radiogenic $^3He/^4He$ (0.5–6.7 R_a) and largely distinct from those found at on-craton settings (4–8.8 R_a). Our findings are consistent with the systematic difference in the $^3He/^4He$ of on– and off-craton continental mantle noted by Day et al. (2015). An important finding from this previous study, and supported by our work, is that a single mean $^3He/^4He$ cannot be attributed to the lithospheric mantle at different tectonic settings as suggested by Gautheron and Moreira (2002). These workers proposed a canonical value of 6.1 ± 0.9 R_a and suggested that this reflected a balance between the He flux from the asthenosphere and the *in-situ* production of radiogenic ^4He in the lithospheric mantle, i.e. a steady state model.

We have advanced on previous work by examining co-variations of $^3He/^4He$ with both major and trace elements in mantle phases from peridotites and pyroxenites. A central result is that fluid-hosted $^3He/^4He$ exhibits systematic relationships with major- and trace-elements hosted in the crystal lattice of mantle olivines and pyroxenes. We suggest that, overall, the variations in $^3He/^4He$ and Mg# exhibited by on– and off-craton mantle largely reflect the amount of melt-extraction in the convecting mantle, and the different amounts of radiogenic ingrowth that occurred at these settings after the melt residues had been incorporated into the continental mantle (Fig. 10). The more radiogenic $^3He/^4He$ signatures found in on– and off-craton mantle may reflect the involvement of recycled oceanic lithosphere. Metasomatic enrichment associated with fluids results in the formation of amphibole and clinopyroexene with relatively high Th and U, which increases ingrowth of ^4He and causes minor scatter on the global lithospheric mantle array on $^3He/^4He$ vs major element plots.

Our new findings highlight the influence of material derived from the lithospheric mantle on the $^3He/^4He$ of continental magmas. The dominantly radiogenic $^3He/^4He$ signatures observed for kimberlites that have ascended through thick, ancient cratonic lithospheric mantle reflect the high propensity of their parental melts to assimilate and digest orthopyroxene (Russell et al., 2012); in many cases this has resulted in overprinting of the initial high $^3He/^4He$ expected for kimberlites derived from the convecting mantle. This is distinct to younger and thinner off-craton mantle, which has a lower propensity to be assimilated by ascending basaltic magmas and enables them to preserve less radiogenic $^3He/^4He$ signatures.

Our observation that $^3He/^4He$ hosted in fluid inclusions in continental lithospheric mantle phases has remained largely undisturbed between metasomatic events (except above convergent margins) is of importance to global cycles of helium and also co-existing volatile species which behave similarly (e.g., CO_2, CH_4, H_2O; (Frezzotti et al., 2012); these may also become trapped in the continental mantle and isolated from global volatile cycles operating between Earth's deep mantle and atmospheric reservoirs on potentially billion-year time scales.

8. Data availability

Data are available through Mendeley Data at https://data.mendeley.com/datasets/wyds2h3mrj/1

CRediT authorship contribution statement

S.A. Gibson: Writing – review & editing, Writing – original draft, Visualization, Supervision, Resources, Project administration, Methodology, Investigation, Funding acquisition, Formal analysis, Data curation, Conceptualization. **J.C. Crosby:** Writing – original draft, Visualization, Methodology, Investigation, Formal analysis, Data curation. **J.A.F. Day:** Methodology. **F.M. Stuart:** Writing – review & editing, Supervision, Resources, Methodology, Investigation, Conceptualization. **L. DiNicola:** Methodology. **T.R. Riley:** Writing – review & editing, Supervision, Conceptualization.

Declaration of competing interest

The authors declare that they have no known competing financial interests or personal relationships that could have appeared to influence the work reported in this paper.

Acknowledgements

We thank Dan McKenzie and the Natural History Museum (UK) for providing many of the mantle xenoliths analysed in this study. Additional samples are from the JB Dawson collection housed in the Dept of Earth Sciences, University of Cambridge and curated by SAG. We are grateful to Iris Buisman for assistance with electron microprobe. Our manuscript has benefitted significantly from the detailed reviews of James Day and two anonymous reviewers. We thank them for their constructive comments and also Manuel Moreira for editorial handling of our manuscript. This work was supported by Natural Environment Research Council grant NE/L002507/1 awarded to JCC.

Appendix A. Supplementary material

The Supplementary Material contains supporting information outlining sample localities, petrographic information, micro-analytical techniques (EMPA, LA-ICP-MS, SEM) and $^3He/^4He$ analysis. The modal mineralogy of the mantle xenoliths, major element composition of olivine, orthopyroxene, clinopyroxene, spinel, garnet, amphibole, phlogopite, and ilmenite obtained by EMPA, and calculated whole-rock major element data of mantle xenoliths are provided as electronic tables. Spreadsheets with the closed-system $^3He/^4He$ evolution model and binary mixing model are also in the Supplementary Material. Supplementary material to this article can be found online at https://doi.org/10.1016/j.gca.2024.09.009.

References

Allègre, C.J., Moreira, M., Staudacher, T., 1995. $^4He/^3He$ dispersion and mantle convection. Geophys. Res. Lett. 22, 2325–2328.

Andersen, T., Neumann, E.-R., 2001. Fluid inclusions in mantle xenoliths. Lithos 55, 301–320.

Arai, S., 1994. Characterization of spinel peridotites by olivine-spinel compositional relationships: Review and interpretation. Chem. Geol. 113, 191–204.

Barfod, D.N., Ballentine, C.J., Halliday, A.N., Fitton, J.G., 1999. Noble gases in the Cameroon line and the He, Ne, and Ar isotopic compositions of high μ (HIMU) mantle. 104, 29509–29527.

Barry, P.H., et al., 2015. Helium isotopic evidence for modification of the cratonic lithosphere during the Permo-Triassic Siberian flood basalt event. Lithos 216–217, 73–80.
Barry, P.H., Broadley, M.W., 2021. Nitrogen and noble gases reveal a complex history of metasomatism in the Siberian lithospheric mantle. Earth Planet. Sci. Lett. 556, 116707.
Barry, T.L., Saunders, A.D., Kempton, P.D., Windley, B.F., Pringle, M.S., Dorjnamjaa, D., Saandar, S., 2003. Petrogenesis of Cenozoic basalts from Mongolia: Evidence for the role of asthenospheric versus metasomatized lithospheric mantle sources. J. Petrol. 44, 55–91.
Beccaluva, L., Bianchini, G., Ellam, R.M., Natali, C., Santato, A., Siena, F. , Stuart, F.M., 2011. Peridotite xenoliths from Ethiopia: Inferences about mantle processes from plume to rift settings. Geological Society of America Special Papers. Geological Society of America, 77–104.
Bell, D.R., Grégoire, M., Grove, T.L., Chatterjee, N., Carlson, R.W., Buseck, P.R., 2005. Silica and volatile-element metasomatism of Archean mantle: a xenolith-scale example from the Kaapvaal Craton. Contrib. Miner. Petrol. 150, 251–267.
Berkesi, M., Czuppon, G., Szabó, C., Kovács, I., Ferrero, S., Boiron, M.-C., Peiffert, C., 2019. Pargasite in fluid inclusions of mantle xenoliths from northeast Australia (Mt. Quincan): evidence of interaction with asthenospheric fluid. Chem. Geol. 508, 182–196.
Bernstein, S., Kelemen, P.B., Hanghoj, K., 2007. Consistent olivine Mg# in cratonic mantle reflects Archean mantle melting to the exhaustion of orthopyroxene. Geology 35, 459–462.
Blundy, J., Dalton, J., 2000. Experimental comparison of trace element partitioning between clinopyroxene and melt in carbonate and silicate systems, and implications for mantle metasomatism. Contrib. Miner. Petrol. 139, 356–371.
Boyd, F.R., 1989. Compositional distinction between oceanic and cratonic lithosphere. Earth Planet. Sci. Lett. 96, 15–26.
Brandon, A.D., Draper, D.S., 1996. Constraints on the origin of the oxidation state of mantle overlying subduction zones: An example from Simcoe, Washington, USA. Geochim. Cosmochim. Acta 60, 1739–1749.
Brown, R.J., Manya, S., Buisman, I., Fontana, G., Field, M., Niocaill, C.M., Sparks, R.S.J., Stuart, F.M., 2012. Eruption of kimberlite magmas: physical volcanology, geomorphology and age of the youngest kimberlitic volcanoes known on earth (the Upper Pleistocene/Holocene Igwisi Hills volcanoes, Tanzania). Bull. Volcanol. 74, 1621–1643.
Burton, K.W., Schiano, P., Birck, J.-L., Allègre, C.J., Rehkämper, M., Halliday, A.N., Dawson, J.B., 2000. The distribution and behaviour of rhenium and osmium amongst mantle minerals and the age of the lithospheric mantle beneath Tanzania. Earth Planet. Sci. Lett. 183, 93–106.
Canil, D., O'Neill, H.St. C., Pearson, D.G., Rudnick, R.L., McDonough, W.F., Carswell, D. A., 1994. Ferric iron in peridotites and mantle oxidation states. Earth Planet. Sci. Lett. 123, 205–220.
Carlson, R.W., Ionov, D.A., 2019. Compositional characteristics of the MORB mantle and bulk silicate earth based on spinel peridotites from the Tariat Region, Mongolia. Geochim. Cosmochim. Acta 257, 206–223.
Carracedo, A., Rodés, Á., Smellie, J.L., Stuart, F.M., 2019. Episodic erosion in West Antarctica inferred from cosmogenic 3He and 10Be in olivine from Mount Hampton. Geomorphology 327, 438–445.
Class, C., Goldstein, S.L., 1997. Plume-lithosphere interactions in the ocean basins: constraints from the source mineralogy. Earth Planet. Sci. Lett. 150, 245–260.
Cohen, R.S., O'Nions, R.K., Dawson, J.B., 1984. Isotope geochemistry of xenoliths from East Africa: Implications for development of mantle reservoirs and their interaction. Earth Planet. Sci. Lett. 68, 209–220.
Coltorti, M., Bonadiman, C., Hinton, R.W., Siena, F., Upton, B.G.J., 1999. Carbonatite Metasomatism of the Oceanic Upper Mantle: Evidence from Clinopyroxenes and Glasses in Ultramafic Xenoliths of Grande Comore, Indian Ocean. J. Petrol. 40, 133–165.
Correale, A., Martelli, M., Paonita, A., Rizzo, A., Brusca, L., Scribano, V., 2012. New evidence of mantle heterogeneity beneath the Hyblean Plateau (southeast Sicily, Italy) as inferred from noble gases and geochemistry of ultramafic xenoliths. Lithos 132–133, 70–81.
Correale, A., Paonita, A., Rizzo, A., Grassa, F., Martelli, M., 2015. The carbon-isotope signature of ultramafic xenoliths from the Hyblean Plateau (southeast Sicily, Italy): Evidence of mantle heterogeneity. Geochem. Geophys. Geosyst. 16, 600–611.
Correale, A., Pelorosso, B., Rizzo, A.L., Coltorti, M., Italiano, F., Bonadiman, C., Giacomoni, P.P., 2019. The nature of the West Antarctic Rift System as revealed by noble gases in mantle minerals. Chem. Geol. 524, 104–118.
Czuppon, G., Matsumoto, T., Handler, M.R., Matsuda, J., 2009. Noble gases in spinel peridotite xenoliths from Mt Quincan, North Queensland, Australia: Undisturbed MORB-type noble gases in the subcontinental lithospheric mantle. Chem. Geol. 266, 19–28.
Dawson, P.J.B., 1980. The Megacryst Suite. Kimberlites and Their Xenoliths. Springer, Berlin Heidelberg, pp. 190–199.
Dawson, J.B., 1984. Contrasting types of upper-mantle metasomatism? In: Kornprobst, J. (Ed.), Developments in Petrology. Elsevier, pp. 289–294.
Dawson, J.B., 2008. The Gregory Rift Valley and Neogene-Recent Volcanoes of Northern Tanzania. Geological Society, London, Memoirs, p. 33.
Day, J.M.D., Hilton, D.R., Pearson, D.G., Macpherson, C.G., Kjarsgaard, B.A., Janney, P. E., 2005. Absence of a high time-integrated $^{3}He/(U+Th)$ source in the mantle beneath continents. *Geology*. Geoscienceworld 33, 733–736.
Day, J.M.D., Barry, P.H., Hilton, D.R., Burgess, R., Pearson, D.G., Taylor, L.A., 2015. The helium flux from the continents and ubiquity of low-$^{3}He/^{4}He$ recycled crust and lithosphere. Geochim. Cosmochim. Acta 153, 116–133.
Day, J.M.D., Harvey, R.P., Hilton, D.R., 2019. Melt-modified lithosphere beneath Ross Island and its role in the tectono-magmatic evolution of the West Antarctic Rift System. Chem. Geol. 518, 45–54.
Day, J.M.D., Pearson, D.G., Kjarsgaard, B.A., Barker, A.K., Nowell, G.M., Joyce, N., Lowry, D., Sarkar, C., Harrison, C., 2023. Early Eocene Arctic volcanism from carbonate-metasomatized mantle. Contrib. Miner. Petrol. 178, 91.
Dodson, A., Brandon, A.D., 1999. Radiogenic helium in xenoliths from Simcoe, Washington, USA: implications for metasomatic processes in the mantle wedge above subduction zones. Chem. Geol. 160, 371–385.
Dodson, A., DePaolo, D.J., Kennedy, B.M., 1998. Helium isotopes in lithospheric mantle: evidence from tertiary basalts of the western USA. Geochim. Cosmochim. Acta 62, 3775–3787.
Dunai, T.J., Baur, H., 1995. Helium, neon, and argon systematics of the European subcontinental mantle: Implications for its geochemical evolution. Geochim. Cosmochim. Acta 59, 2767–2783.
Dunai, T.J., Porcelli, D., 2002. Storage and Transport of Noble Gases in the Subcontinental Lithosphere. Rev. Mineral. Geochem. 47, 371–409.
Faccini, B., Rizzo, A.L., Bonadiman, C., Ntaflos, T., Seghedi, I., Grégoire, M., Ferretti, G., Coltorti, M., 2020. Subduction-related melt refertilisation and alkaline metasomatism in the Eastern Transylvanian Basin lithospheric mantle: Evidence from mineral chemistry and noble gases in fluid inclusions. Lithos 364–365, 105516.
Foeken, J.P.T., Day, S., Stuart, F.M., 2009. Cosmogenic 3He exposure dating of the Quaternary basalts from Fogo, Cape Verdes: Implications for rift zone and magmatic reorganisation. Quat. Geochronol. 4, 37–49.
Frezzotti, M.L., Ferrando, S., Tecce, F., Castelli, D., 2012. Water content and nature of solutes in shallow-mantle fluids from fluid inclusions. Earth Planet. Sci. Lett. 351–352, 70–83.
Gaffney, A.M., Blichert-Toft, J., Nelson, B.K., Bizzarro, M., Rosing, M., Albarède, F., 2007. Constraints on source-forming processes of West Greenland kimberlites inferred from Hf–Nd isotope systematics. Geochim. Cosmochim. Acta 71, 2820–2836.
Gautheron, C., Moreira, M., 2002. Helium signature of the subcontinental lithospheric mantle. Earth Planet. Sci. Lett. 199, 39–47.
Gautheron, C., Moreira, M., Allègre, C., 2005. He, Ne and Ar composition of the European lithospheric mantle. Chem. Geol. 217, 97–112.
Gibson, S.A., 2008. Melt depletion and enrichment of the Kaapvaal craton: Evidence from Finsch peridotites. J. Petrol. 1817–1852.
Gibson, S.A., McKenzie, D., 2023. On the role of the lithospheric mantle in global volatile cycles. Earth Planet. Sci. Lett. 602, 117946.
Gibson, S.A., McMahon, S.C., Day, J.A., Dawson, J.B., 2013. Highly-refractory lithospheric mantle beneath the Tanzanian Craton: evidence from Lashaine pre-metasomatic garnet-bearing peridotites. J. Petrol. 54, 1503–1546.
Gibson, S.A., Rooks, E., Day, J.A., Petrone, C.M., Leat, P.T., 2020. The role of sub-continental mantle as both "sink" and "source" in deep Earth volatile cycles. Geochim. Cosmochim. Acta 275, 140–162.
Giuliani, A., Koornneef, J.M., Barry, P., Will, P., Busemann, H., Maden, C., Maas, R., Greig, A., Davies, G.R., 2020b. A preliminary assessment of the application of Sr, Nd, Pb, He and N isotope analysis to fluid inclusions in kimberlite olivine: a new approach to trace deep-mantle sources. paper presented at the EGU General Assembly Conference Abstracts 5267.
Giuliani, A. et al., 2020a. Kimberlite genesis from a common carbonate-rich primary melt modified by lithospheric mantle assimilation. Science Advances. American Association for the Advancement of Science 6, eaaz0424.
Graham, D.W., 2002. Noble gas isotope geochemistry of mid-ocean ridge and ocean island basalts: Characterization of mantle source reservoirs. Rev. Mineral. Geochem. 47, 247–317.
Halldórsson, S.A., et al., 2022. Evidence from gas-rich ultramafic xenoliths for superplume-derived recycled volatiles in the East African sub-continental mantle. Chem. Geol. 589, 120682.
Halldórsson, S.A., Hilton, D.R., Scarsi, P., Abebe, T., Hopp, J., 2014. A common mantle plume source beneath the entire East African Rift System revealed by coupled helium-neon systematics. Geophys. Res. Lett. 41, 2304–2311.
Harvey, J., Dale, C.W., Gannoun, A., Burton, K.W., 2011. Osmium mass balance in peridotite and the effects of mantle-derived sulphides on basalt petrogenesis. Geochim. Cosmochim. Acta 75, 5574–5596.
Heckel, C., Woodland, A.B., Linckens, J., Gibson, S.A., Seitz, H.-M., 2022. Sheared peridotites from Kimberley (Kaapvaal Craton, RSA): Record of multiple metasomatic events accompanied with deformation. J. Petrol. 63, egac096.
Heinonen, J.S., Kurz, M.D., 2015. Low-$^{3}He/^{4}He$ sublithospheric mantle source for the most magnesian magmas of the Karoo large igneous province. Earth Planet. Sci. Lett. 426, 305–315.
Hermann, J., Rubatto, D., 2009. Accessory phase control on the trace element signature of sediment melts in subduction zones. Chem. Geol. 265, 512–526.
Herzberg, C., 2004. Geodynamic information in peridotite petrology. J. Petrol. 45, 2507–2530.
Herzberg, C., Condie, K., Korenaga, J., 2010. Thermal history of the Earth and its petrological expression. Earth Planet. Sci. Lett. 292, 79–88.
Herzberg, C., Rudnick, R., 2012. Formation of cratonic lithosphere: An integrated thermal and petrological model. Lithos 149, 4–15.
Hilton, D.R., Fischer, T.P., Marty, B., 2002. Noble gases and volatile recycling at subduction zones. Rev. Mineral. Geochem. 47, 319–370.
Hilton, D.R., Halldórsson, S.A., Barry, P.H., Fischer, T.P., de Moor, J.M., Ramirez, C.J., Mangasini, F., Scarsi, P., 2011. Helium isotopes at Rungwe Volcanic Province, Tanzania, and the origin of East African Plateaux. Geophys. Res. Lett. 38.

Hoke, L., Poreda, R., Reay, A., Weaver, S.D., 2000. The subcontinental mantle beneath southern New Zealand, characterised by helium isotopes in intraplate basalts and gas-rich springs. Geochim. Cosmochim. Acta 64, 2489–2507.
Horton, F., Asimow, P.D., Farley, K.A., Curtice, J., Kurz, M.D., Blusztajn, J., Biasi, J.A., Boyes, X.M., 2023. Highest terrestrial $^{3}He/^{4}He$ credibly from the core. *Nature*. Nature Publishing Group 623, 90–94.
Howarth, G.H., Barry, P.H., Pernet-Fisher, J.F., Baziotis, I.P., Pokhilenko, N.P., Pokhilenko, L.N., Bodnar, R.J., Taylor, L.A., Agashev, A.M., 2014. Superplume metasomatism: Evidence from Siberian mantle xenoliths. Lithos 184–187, 209–224.
Jackson, C.J., Gibson, S.A., 2023. Build-up of multiple volatiles in Earth's continental keels: implications for craton stability. Earth Planet. Sci. Lett. 611, 118134.
Jalowitzki, T., Sumino, H., Conceição, R.V., Orihashi, Y., Nagao, K., Bertotto, G.W., Balbinot, E., Schilling, M.E., Gervasoni, F., 2016. Noble gas composition of subcontinental lithospheric mantle: an extensively degassed reservoir beneath Southern Patagonia. Earth Planet. Sci. Lett. 450, 263–273.
Janney, P.E., Roex, A.P.L., Carlson, R.W., Viljoen, K.S., 2002. A chemical and multi-isotope study of the Western Cape olivine melilitite province, South Africa: implications for the sources of kimberlites and the origin of the HIMU signature in Africa. J. Petrol. 43, 2339–2370.
Kelemen, P.B., Hart, S.R., Bernstein, S., 1998. Silica enrichment in the continental upper mantle via melt/rock reaction. Earth Planet. Sci. Lett. 164, 387–406.
Kessel, R., Schmidt, M.W., Ulmer, P., Pettke, T., 2005. Trace element signature of subduction-zone fluids, melts and supercritical liquids at 120–180 km depth. Nature 437, 724–727.
Kim, K.H., Nagao, K., Tanaka, T., Sumino, H., Nakamura, T., Okuno, M., Lock, J.B., Youn, J.S., Song, J., 2005. He-Ar and Nd-Sr isotopic compositions of ultramafic xenoliths and host alkali basalts from the Korean peninsula. Geochem. J. 39, 341–356.
Kobayashi, M., et al., 2019. Halogen heterogeneity in the lithosphere and evolution of mantle halogen abundances inferred from intraplate mantle xenoliths. Geochem. Geophys. Geosyst.
Konrad, K., Graham, D.W., Thornber, C.R., Duncan, R.A., Kent, A.J.R., Al-Amri, A.M., 2016. Asthenosphere–lithosphere interactions in Western Saudi Arabia: Inferences from $^{3}He/^{4}He$ in xenoliths and lava flows from Harrat Hutaymah. Lithos 248–251, 339–352.
Kurz, M.D., Geist, D.J., 1999. Dynamics of the Galápagos hotspot from helium isotope geochemistry. Geochim. Cosmochim. Acta 63, 4139–4156.
Langmuir, C.H., Vocke, R.D., Hanson, G.N., Hart, S.R., 1978. A general mixing equation with applications to Icelandic basalts. Earth Planet. Sci. Lett. 37, 380–392.
Leat, P.T., Ross, A.J., Gibson, S.A., 2023. Ultramafic mantle xenoliths in the Late Cenozoic volcanic rocks of the Antarctic Peninsula and Jones Mountains, West Antarctica. Geological Society, London Memoirs. the Geological Society of London 56, 101–114.
Lippolt, H., 1983. Distribution of volcanic activity in space and time. Plateau Uplift. Heidelberg: Springer-Verlag.
Martelli, M., Bianchini, G., Beccaluva, L., Rizzo, A., 2011. Helium and argon isotopic compositions of mantle xenoliths from Tallante and Calatrava, Spain. J. Volcanol. Geoth. Res. 200, 18–26.
Marty, B., Tolstikhin, I., Kamensky, I.L., Nivin, V., Balaganskaya, E., Zimmermann, J.-L., 1998. Plume-derived rare gases in 380 Ma carbonatites from the Kola region (Russia) and the argon isotopic composition in the deep mantle. Earth Planet. Sci. Lett. 164, 179–192.
Marty, B., Tolstikhin, I.N., 1998. CO_2 fluxes from mid-ocean ridges, arcs and plumes. Chem. Geol. 145, 233–248.
Matsumoto, T., Honda, M., McDougall, I., Yatsevich, I., O'Reilly, S.Y., 1997. Plume-like neon in a metasomatic apatite from the Australian lithospheric mantle. Nature 388, 162–164.
Matsumoto, T., Honda, M., Mcdougall, I., O'Reilly, S.Y., 1998. Noble gases in anhydrous lherzolites from the newer volcanics, southeastern Australia: a MORB-like reservoir in the subcontinental mantle. Geochim. Cosmochim. Acta 62, 2521–2533.
McIntyre, T., Kublik, K., Currie, C., Pearson, D.G., 2021. Heat generation in cratonic mantle roots—New trace element constraints from mantle xenoliths and implications for cratonic geotherms. Geochem. Geophys. Geosyst., e2021GC009691
McKenzie, D., 1989. Some remarks on the movement of small melt fractions in the mantle. Earth Planet. Sci. Lett. 95, 53–72.
McKenzie, D., Bickle, M.J., 1988. The volume and composition of melt generated by extension of the lithosphere. J. Petrol. 29, 625–679.
Menzies, M.A., 1983. Mantle ultramafic xenoliths in alkaline magmas: evidence for mantle heterogeneity modified by magmatic activity. Continental Basalts and Mantle Xenoliths, eds Hawkesworth C.J. & Norry M.J., publ. Shiva, Nantwich, pp. 92–110.
Mercier, J.-C.-C., Nicolas, A., 1975. Textures and fabrics of upper-mantle peridotites as illustrated by xenoliths from basalts. J. Petrol. 16, 454–487.
Nardini, I., Armienti, P., Rocchi, S., Dallai, L., Harrison, D., 2009. Sr–Nd–Pb–He–O isotope and geochemical constraints on the genesis of Cenozoic magmas from the West Antarctic Rift. J. Petrol. 50, 1359–1375.
O'Reilly, S.Y., Griffin, W.L. Mantle Metasomatism. Metasomatism and the Chemical Transformation of Rock. Springer Berlin Heidelberg, Berlin, Heidelberg, pp. 471–533.
Oller, B., Day, J.M.D., Driscoll, N.W., Lonsdale, P.F., 2022. Generation of Continental Lithospheric Mantle by Tectonic Isolation of Oceanic Plate. Geochem. Geophys. Geosyst. 23, e2022GC010353.
Pearson, D.G., Carlson, R.W., Shirey, S.B., Boyd, F.R., Nixon, P.H., 1995a. Stabilisation of Archaean lithospheric mantle: a Re-Os isotope study of peridotite xenoliths from the Kaapvaal craton. Earth Planet. Sci. Lett. 134, 341–357.
Pearson, D.G., Shirey, S.B., Carlson, R.W., Boyd, F.R., Pokhilenko, N.P., Shimizu, N., 1995b. Re-Os, Sm-Nd, and Rb-Sr isotope evidence for thick Archaean lithospheric mantle beneath the Siberian craton modified by multistage metasomatism. Geochim. Cosmochim. Acta 59, 959–977.
Pearson, D.G., Scott, J.M., Liu, J., Schaeffer, A.J., Wang, L.H., van Hunen, J., Szilas, K., Chako, T., Kelemen, P.B., 2021. Deep Continental Roots and Cratons 596, 199–210.
Pearson, D.G., Wittig, N., 2014. The formation and evolution of cratonic mantle lithosphere - evidence from mantle xenoliths. Treatise in Geochemistry. Elsevier 255–292.
Pintér, Z., Foley, S.F., Yaxley, G.M., Rosenthal, A., Rapp, R.P., Lanati, A.W., Rushmer, T., 2021. Experimental investigation of the composition of incipient melts in upper mantle peridotites in the presence of CO_2 and H_2O. Lithos 396–397, 106224.
Porcelli, D., Elliott, T., 2008. The evolution of He Isotopes in the convecting mantle and the preservation of high 3He/4He ratios. Earth Planet. Sci. Lett. 269, 175–185.
Priestley, K., McKenzie, D., 2013. The relationship between shear wave velocity, temperature, attenuation and viscosity in the shallow part of the mantle. Earth Planet. Sci. Lett. 381, 78–91.
Reid, M.R., Graham, D.W., 1996. Resolving lithospheric and sub-lithospheric contributions to helium isotope variations in basalts from the southwestern US. Earth Planet. Sci. Lett. 144, 213–222.
Richter, F.M., 1988. A major change in the thermal state of the Earth at the Archean-Proterozoic boundary: consequences for the nature and preservation of continental lithosphere. J. Petrol. Special Lithosphere Issue 39–52.
Rizzo, A. L., Pelorosso, B., Coltorti, M., Ntaflos, T., Bonadiman, C., Matusiak-Małek, M., Italiano, F.M., Bergonzoni, G., 2018. Geochemistry of noble gases and CO2 in fluid inclusions from lithospheric mantle beneath Wilcza Góra (Lower Silesia, Southwest Poland). Frontiers in Earth Science. Frontiers 6.
Rizzo, A.L., Faccini, B., Casetta, F., Faccincani, L., Ntaflos, T., Italiano, F., Coltorti, M., 2021. Melting and metasomatism in West Eifel and Siebengebirge sub-continental lithospheric mantle: Evidence from concentrations of volatiles in fluid inclusions and petrology of ultramafic xenoliths. Chem. Geol. 581, 120400.
Russell, J.K., Porritt, L.A., Lavallée, Y., Dingwell, D.B., 2012. Kimberlite ascent by assimilation-fuelled buoyancy. Nature 481, 352–356.
Salters, V.J.M., Stracke, A., 2004. Composition of the depleted mantle. Geochem. Geophys. Geosyst. 5, 2004.
Sapienza, G., Hilton, D.R., Scribano, V., 2005. Helium isotopes in peridotite mineral phases from Hyblean Plateau xenoliths (south-eastern Sicily, Italy). Chem. Geol. 219, 115–129.
Scott, J.M., Liu, J., Pearson, D.G., Harris, G.A., Czertowicz, T.A., Woodland, S.J., Riches, A.J.V., Luth, R.W., 2019. Continent stabilisation by lateral accretion of subduction zone-processed depleted mantle residues; insights from Zealandia. Earth Planet. Sci. Lett. 507, 175–186.
Servali, A., Korenaga, J., 2018. Oceanic origin of continental mantle lithosphere. Geology 46, 1047–1050.
Sgualdo, P., Aviado, K., Beccaluva, L., Bianchini, G., Blichert-Toft, J., Bryce, J.G., Graham, D.W., Natali, C., Siena, F., 2015. Lithospheric mantle evolution in the Afro-Arabian domain: Insights from Bir Ali mantle xenoliths (Yemen). Tectonophysics 650, 3–17.
Shu, Q., Brey, G.P., Pearson, D.G., Liu, J., Gibson, S.A., Becker, H., 2019. The evolution of the Kaapvaal craton: a multi-isotopic perspective from lithospheric peridotites from Finsch diamond mine. Precambr. Res. 331, 105380.
Simon, N.S.C., Carlson, R.W., Pearson, D.G., Davies, G.R., 2007. The origin and evolution of the Kaapvaal cratonic lithospheric mantle. J. Petrol. 48, 589–625.
Smye, A.J., Jackson, C.R.M., Konrad-Schmolke, M., Hesse, M.A., Parman, S.W., Shuster, D.L., Ballentine, C.J., 2017. Noble gases recycled into the mantle through cold subduction zones. Earth Planet. Sci. Lett. 471, 65–73.
Stachel, T., Harris, J.W., 2008. The origin of cratonic diamonds — constraints from mineral inclusions. Ore Geol. Rev. 34, 5–32.
Starkey, N.A., Stuart, F.M., Ellam, R.M., Fitton, J.G., Basu, S., Larsen, L.M., 2009. Helium isotopes in early Iceland plume picrites: Constraints on the composition of high 3He/4He mantle. Earth and Planetary Science Letters 277, 91–100.
Stuart, F.M., Ellam, R.M., Harrop, P.J., Fitton, J.G., Bell, B.R., 2000. Constraints on mantle plumes from the helium isotopic composition of basalts from the British Tertiary Igneous Province. Earth Planet. Sci. Lett. 177, 273–285.
Stuart, F.M., Lass-Evans, S., Godfrey Fitton, J., Ellam, R.M., 2003. High $^{3}He/^{4}He$ ratios in picritic basalts from Baffin Island and the role of a mixed reservoir in mantle plumes. Nature 424, 57–59.
Su, F., Xiao, Y., He, H., Su, B., Wang, Y., Zhu, R., 2014. He and Ar isotope geochemistry of pyroxene megacrysts and mantle xenoliths in Cenozoic basalt from the Changle-Linqu area in western Shandong. Chin. Sci. Bull. 59, 396–411.
Sumino, H., Kaneoka, I., Matsufuji, K., Sobolev, A.V., 2006. Deep mantle origin of kimberlite magmas revealed by neon isotopes. Geophys. Res. Lett. 33.
Tachibana, Y., Kaneoka, I., Gaffney, A., Upton, B., 2006. Ocean-island basalt–like source of kimberlite magmas from West Greenland revealed by high $^{3}He/^{4}He$ ratios. Geology 34, 273–276.
Tainton, K., McKenzie, D., 1994. The generation of kimberlites, lamproites, and their source rocks. J. Petrol. 35, 787–817.
Tappe, S., Pearson, D.G., Nowell, G., Nielsen, T., Milstead, P., Muehlenbachs, K., 2011. A fresh isotopic look at Greenland kimberlites: Cratonic mantle lithosphere imprint on deep source signal. Earth and Planetary Science Letters 305, 235–248.
Tolstikhin, I.N., et al., 2002. Rare gas isotopes and parent trace elements in ultrabasic-alkaline-carbonatite complexes, Kola Peninsula: identification of lower mantle plume component. Geochim. Cosmochim. Acta 66, 881–901.
Trull, T.W., Kurz, M.D., 1993. Experimental measurements of ^{3}He and ^{4}He mobility in olivine and clinopyroxene at magmatic temperatures. Geochim. Cosmochim. Acta 57, 1313–1324.

Walker, R.J., Carlson, R.W., Shirey, S.B., Boyd, F.R., 1989. Os, Sr, Nd, and Pb isotope systematics of southern African peridotite xenoliths: Implications for the chemical evolution of subcontinental mantle. Geochim. Cosmochim. Acta 53, 1583–1595.

Weiss, Y., Kiro, Y., Class, C., Winckler, G., Harris, J.W., Goldstein, S.L., 2021. Helium in diamonds unravels over a billion years of craton metasomatism. *Nat. Commun.*. Nature Publishing Group 12, 2667.

Willcox, A., Buisman, I., Sparks, R.S.J., Brown, R.J., Manya, S., Schumacher, J.C., Tuffen, H., 2015. Petrology, geochemistry and low-temperature alteration of lavas and pyroclastic rocks of the kimberlitic Igwisi Hills volcanoes, Tanzania. Chem. Geol. 405, 82–101.

Wilshire, H.G., Meyer, C.E., Nakata, J.K., Calk, L.C., Shervais, J.W., Nielson, J.E., Schwarzman, E.C., 1988. Mafic and ultramafic xenoliths from volcanic rocks of the western United States. United States Geological Survey.

Workman, R.K., Hart, S.R., 2005. Major and trace element composition of the depleted MORB mantle (DMM). Earth Planet. Sci. Lett. 231, 53–72.

Xu, Q., Liu, J., He, H., Zhang, Y., 2019. Nature and evolution of the lithospheric mantle revealed by water contents and He-Ar isotopes of peridotite xenoliths from Changbaishan and Longgang basalts in Northeast China. Science Bulletin 64, 1325–1335.

Yamamoto, J., Otsuka, K., Ohfuji, H., Ishibashi, H., Hirano, N., Kagi, H., 2011. Retentivity of CO_2 in fluid inclusions in mantle minerals. Eur. J. Mineral. 23, 805–815.

Zhang, Q., Morel, M.L.A., Liu, J., Legros, H., Luguet, A., Viljoen, K.S., Davies, G.R., Pearson, D.G., 2022. Re-healing cratonic mantle lithosphere after the world's largest igneous intrusion: constraints from peridotites erupted by the Premier kimberlite, South Africa. Earth Planet. Sci. Lett. 598, 117838.